Master's Thesis

Investigation on degradation mechanism of $LiNi_{0.6}Co_{0.2}Mn_{0.2}O_2$ bi-modal cathode materials under the high temperature

Seulgi Shin

Department of Energy Engineering

(Energy Engineering)

Graduate School of UNIST

2019

Investigation on degradation mechanism of $LiNi_{0.6}Co_{0.2}Mn_{0.2}O_2$ bi-modal cathode materials under the high temperature

Seulgi Shin

Department of Energy Engineering
(Energy Engineering)

Graduate School of UNIST

Investigation on degradation mechanism of $LiNi_{0.6}Co_{0.2}Mn_{0.2}O_2$ bi-modal cathode materials under the high temperature

A thesis/dissertation
submitted to the Graduate School of UNIST
in partial fulfillment of the
requirements for the degree of
Master of Science

Seulgi Shin

06/14/2019 of submission

Approved by

Advisor
Jaephil Cho

Investigation on degradation mechanism of $LiNi_{0.6}Co_{0.2}Mn_{0.2}O_2$ bi-modal cathode materials under the high temperature

Seulgi shin

This certifies that the thesis/dissertation of Gil-dong Hong is approved.

06.14.2019

Advisor: Jaephil Cho

Kyeong-Min Jeong

Nam-Soon Choi

Abstract

As batteries have been introduced in electric vehicles (EV) and energy storage system (ESS), bi-modal $Li[Ni_xCo_yMn_z]\ O_2$ (NCM) cathode materials have been highlighted thanks to their high value of volumetric energy density. However, these commercial applications accompany huge amount of heat release during cycles, therefore, the NCM cathode materials in battery system are rapidly deteriorated by a heat transfer. Therefore, in order to prevent cathode degradation under high temperature, researchers have studied on degradation mechanism of the cathode materials such as phase transition, metal dissolution, cation mixing and intra/intergranular cracks.

However, the studies are limited in a microscopic view, which can explain degradation mechanism in a particle scale. In the case of the commercial LiBs, the electrodes with a high thickness are fabricated for achieving high energy density. In this circumstance, the cathode particles are placed in a variety of environment, and particle degradation also unequally occurs according to the particle arrangement. Therefore, investigation on degradation mechanism of the bi-modal NCM cathode should be conducted in a local scale.

Herein, *ex-situ* Raman spectroscopy is utilized as a powerful tool to analysis degradation of bi-modal NCM cathode in a local scale. Correlation with ex-situ Raman spectra and XRD spectra shows that ratio of the Raman peak intensity between $597cm^{-1}(A_{1g}, Ni^{2+}O_6)$ and $547cm^{-1}$ $(A_{1g}, Ni^{3+}O_6)$ is proper as an indicator of electrode degradation. On the basis of our investigation, the main factor of cathode degradation under high temperature related with the degree of particle fraction and the improvements are discussed in detail.

Contents

List of figures

Figure 17. (a) SEM image of the cross-sectional NCM 523 electrode after 400 cycles. Raman spectra from various samples: (1) the average of the pristine electrode; (2) the average of the re-lithiated electrode after 400cycles; (3) the average of aged electrode after 400 cycles; (4) typical shape of average Raman spectra of NCM523.[13]

Figure 18 . Scanning electron microscopy (SEM) images of uni-modal and bi-modal cathode materials; (a) the large-sized NCM (LNCM) particle, (b) the small-sized NCM (SNCM) particle, and (c) the blended NCM cathode materials (BNCM). Voltage profile of (a-c); (d) the LNCM electrode and (e) the SNCM electrode at 3.1g/cc, (f) BNCMs at 3.5g/cc. The electrode density is determined by the particle fraction. (g) The volumetric cathode energy density (Wh L^{-1}) of (d-f).

Figure 19. Particle size distribution (PSD) data of the bi-modal NCM 622 cathode. The particles below the 5um are called by SNCM, and the particles above the 8um are called by LNCM.

Figure 20. Cycle performance of the uni-modal cathodes and bi-modal cathode after 250 cycles under the room temperature.

Figure 21. (a) Voltage profile and (b) cycle performance of the BNCM cathode / graphite full cell at 45°C compared with room temperature. Figure (a) shows the voltage profile about every 100 cycle.

Figure 22. SEM images of the (a) SNCM cathode with the electrode density of3.5 g cm^{-3} and the (b) LNCM cathode with the electrode density of3.1g cm^{-3}. Electrochemical impedance spectroscopy (EIS, c,d) of the uni-modal cathode after the formation (green dot), and the unimodal cathode with the different cathode densities at 3.1g cm^{-3} and 3.5g cm^{-3}, after the cycle retention reached at 80% under the high temperature. (black and red dot)

Figure 23. (a) SEM images of the BNCM cathode with the electrode density ≈ 3.5 g cm^{-3}. (b) EIS graph of the BNCM cathode after the formation (green dot), and the BNCM cathode with the electrode density ≈ 3.5g cm^{-3} after the cycle retention reached at 80%

Figure 24. *Ex- situ* Raman spectra of the NCM 622 cathode between 400 cm^{-1} and 700cm^{-1}

Figure 25. (a) *Ex- situ* Raman spectra of pristine NCM 622 cathode (blue green line) and de-lithiated NCM 622 cathode at 4.3V (blue line). The peaks are compared with pristine $LiNi_{0.33}Co_{0.33}Mn_{0.3}O_2$ (Blue green dot), $LiNiO_2$ (blue dot) cathode materials. (b) Normalized Raman intensity graph of (a), which can be observed at 547cm^{-1} (orange bar) and 597cm^{-1} (blue bar).

Figure 26. Differential capacity curve (dQ/dV) graph of the BNCM cathode at the 1st, 100th, 200th cycles under the high temperature.

Figure 27. (a) Variation of *c*-axis parameter (orange line) and Raman intensity at 597cm^{-1} (orange rod graph) according to the operating potential. (b) Variation of *c*-axis parameter (blue line) and Raman intensity at 547cm^{-1} (blue rod graph) according to the operating potential.

Figure 28. Variation of *a*-axis parameter (green line) and Raman intensity at 484cm^{-1} (green rod graph) according to the operating potential.

List of table

Table 1. Pellet density of the uni-modal NCM, bimodal NCM and single crystalline LCO cathode materials. After the pellet density is measured, severe particle fraction is observed at the LNCM particles

I. Introduction

With the advent of the electric vehicles and large-scale energy storage systems, the lithium-based batteries have received great attention.[1, 14-15] Among various lithium-based batteries such as Li-ion, Li-S, Li-air, and all-solid-state batteries, the Li-ion batteries (LIBs) have been recognized as a promising candidate because of its high energy density and long cycle life.[1, 16] Therefore, improving their performance by modification of the cell components have been the key challenges to satisfy the market demands.

Especially, in order to increase areal capacity in the limited space of the LIBs, many researchers have focused on the improvement of cathode materials. Among the promising cathode materials, $Li[Ni_xCo_yMn_z]O_2$ (NCM) cathodes materials have attracted great attraction because of their high value of volumetric energy density (815Wh L^{-1}).[1] Moreover, the NCM cathodes have the great advantages of enhancing properties by changing the ratio of transition metals (TM). For example, the energy density of the cathodes is closely related to the nickel contents, and the amount of cobalt and manganese ions contribute to the thermal stability and the cycle performance. Through the optimized ratio of the transition metals, the NCM cathode have accomplished high capacity and stability.

However, the NCM cathodes have intrinsic problems to be improved. During the cycles, the randomly orientated primary particles undergo anisotropic volume expansion/contraction.[17] In the meantime, electrolyte can infiltrate into the intergranular cracks between the primary particles and react with the newly exposed surface. This reaction induces side reaction such as metal dissolution, oxygen release, and additional solid electrolyte interphase (SEI).[3, 8] Moreover, batteries can absorb amount of heat release from surroundings, thus, the absorption of heat can accelerate battery degradation. Therefore, in order to improve performance of the commercial LiBs, it is necessary to investigate on the degradation mechanism under high temperature.

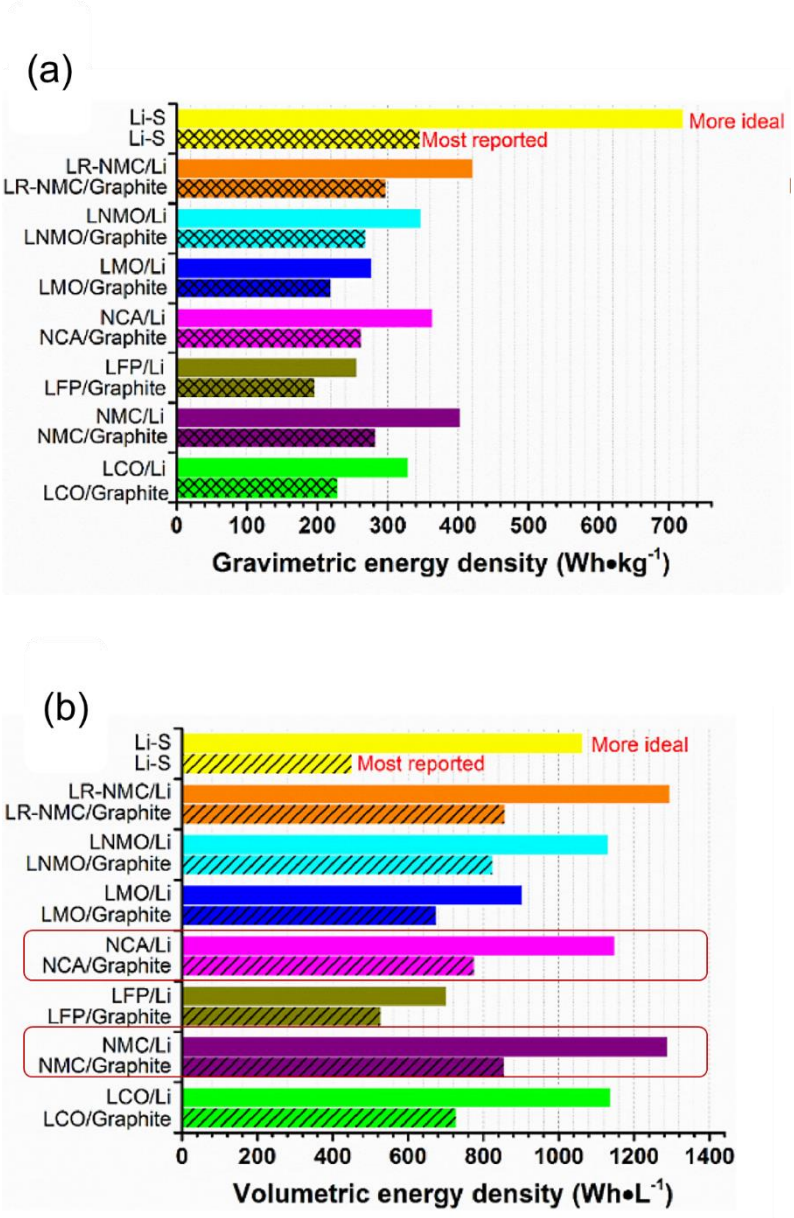

Figure 1. Theoretical gravimetric energy density (Wh kg^{-1}) and volumetric energy density (Wh L^{-1}) of Li-based batteries. The hatched graphs show practical energy density of each full cell.[1]

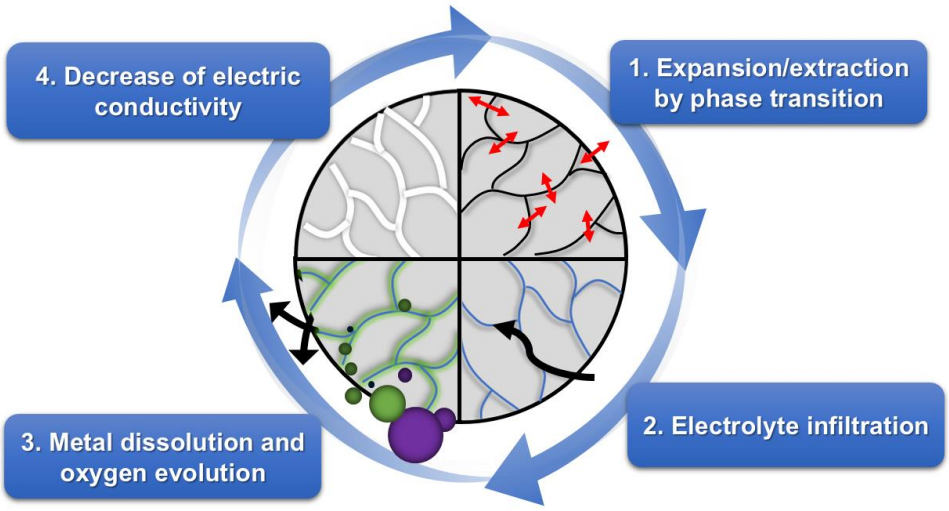

Figure 2. Schematic of the degradation process of the Ni-based cathode materials.

1.1 Fundamental degradation factors of the $Li[Ni_xCo_yMn_z]O_2$ cathodes

Phase transition of the NCM cathodes

At pristine state, layered cathode materials show H1 phase, which undergoes small volume expansion during charge process. However, as repulsion force between oxygen slabs increases during charge, *c*-axis parameter of unit cell increases. As a result, the H1 phase rapidly convert to monoclinic phase (M) and H2 phase. Continuous charge process causes the oxidation number of transition metals to reach 4+. The phenomenon leads to large shrinkage of the *a*-axis of unit cells, and H3 phase is formed. Consequently, repeated expansion and contraction causes each of the primary particles to move apart, and collapses secondary particles.

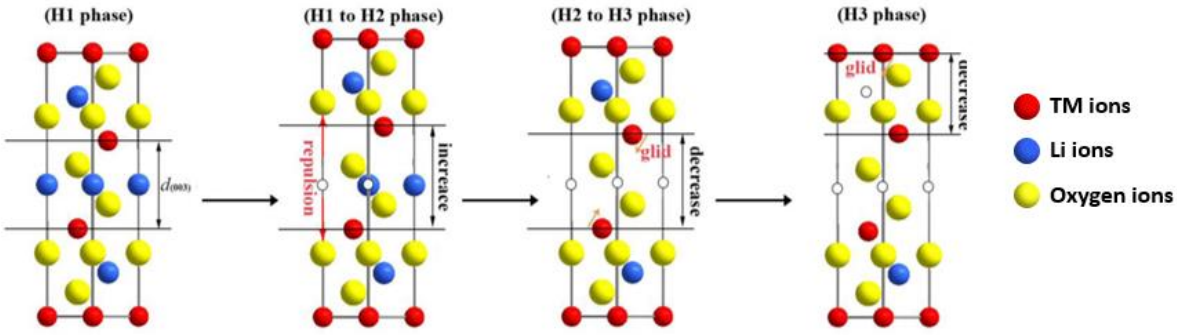

Figure 3. The schematics of phase transition in $Li[Ni_xCo_yMn_z]O_2$ (NCM) cathode during charging process from 3.0 V to 4.5 V.[2]

Phase transition of the NCM cathodes can be demonstrated through the differential capacity analysis (dQ/dV). In Figure 4, first peaks of the NCM cathodes appears at 3.5 V, which shows the intercalation reaction of the graphite anode.[3] Next peaks appear by phase transition from an original hexagonal phase to a monoclinic phase (H1➔M) in layered-structured cathode active material. The significant phase transition from H1 phase to M phase occurs up to 3.8 V, which is clearly observed in all NCM cathode materials regardless of their transition metal composition. However, there are different tendency of phase transition after 3.9V. The $LiNi_{0.8}Co_{0.1}Mn_{0.1}O_2$ (NCM811) cathode materials are clearly transformed to the hexagonal phase (M➔H2).[3] When more lithium ions are extracted from cathode during the de-lithiation reaction, *a/c*- axis parameter

rapidly decreases and new phase, H3, is formed (H2➔H3). In contrast, no significant peaks after 3.8 V are observed in $LiNi_{0.6}Co_{0.2}Mn_{0.2}O_2$ (NCM622) and $LiNi_{0.33}Co_{0.33}Mn_{0.33}O_2$ (NCM111), whose nickel content is much lower than that of NCM 811, which means that phase transition of low-nickel NCM material is hard to be demonstrated in high voltage.

However, as shown from Figure 5, the phase transition of NCM 622 is clearly visualized through *in- operando* XRD pattern by Zheng et al.[4] At 3.8 V, (003), (101), (107), (018) and (113) peaks are split into two peaks, which means appearance of new phase with different inter-spacing value *via* phase conversion. Among the XRD peaks, the (003) and (104) peaks are the important indicators for phase transition because they are directly related with the *a* and *c* lattice parameters of unit cell. During the deep de-lithiation process, the (003) peak moves to low angle until 4.3 V and then, after 4.4 V, (003) peak rapidly shifts to higher angle, and (104) peak is split.[4] This drastic change in two major peaks demonstrates the phase transition from H2 phase to H3 phase.

Moreover, in Figure 6, Rietveld refinement analysis and voltage profile show the cell volume change according to phase transition and the amounts of lithium ions in NCM cathode materials at specific voltage.[4, 18] The H1 phase of $Li_{1-x}Ni_{0.6}Co_{0.2}Mn_{0.2}O_2$ (NCM 622) completely disappears at $x<0.36$, and the volume change at the H1 phase is hardly detected during charge process. However, when more lithium ions are de-intercalated from the lattice structure, the Li-deficient H2 phase disappears at $x<0.73$, which leads to significant cell volume change at least 2% due to the rapid decrease of the cell parameters. At last, severe de-lithiation of layered-structured NCM cathode material causes formation of H3 phase with extreme decrease of unit cell volume, which is induced by drastic decrease of *c*-axis parameter. Structural irreversibility appears during repeated charge and discharge processes with deep state of charge, and finally, it leads to growth of irreversible capacity.[4, 18]

These crystallographic changes not only affect irreversible phase transition in a primary particle, but also bring about crack formation in a secondary particle. Repeat of anisotropic expansion and contraction causes weakening of bond strength between primary particles, and consequent crack formation and isolation of primary particles. As a result, crack formation in secondary particle, loss of electrical conductivity and more severe surface side reactions occur, which increase dead space in active material.

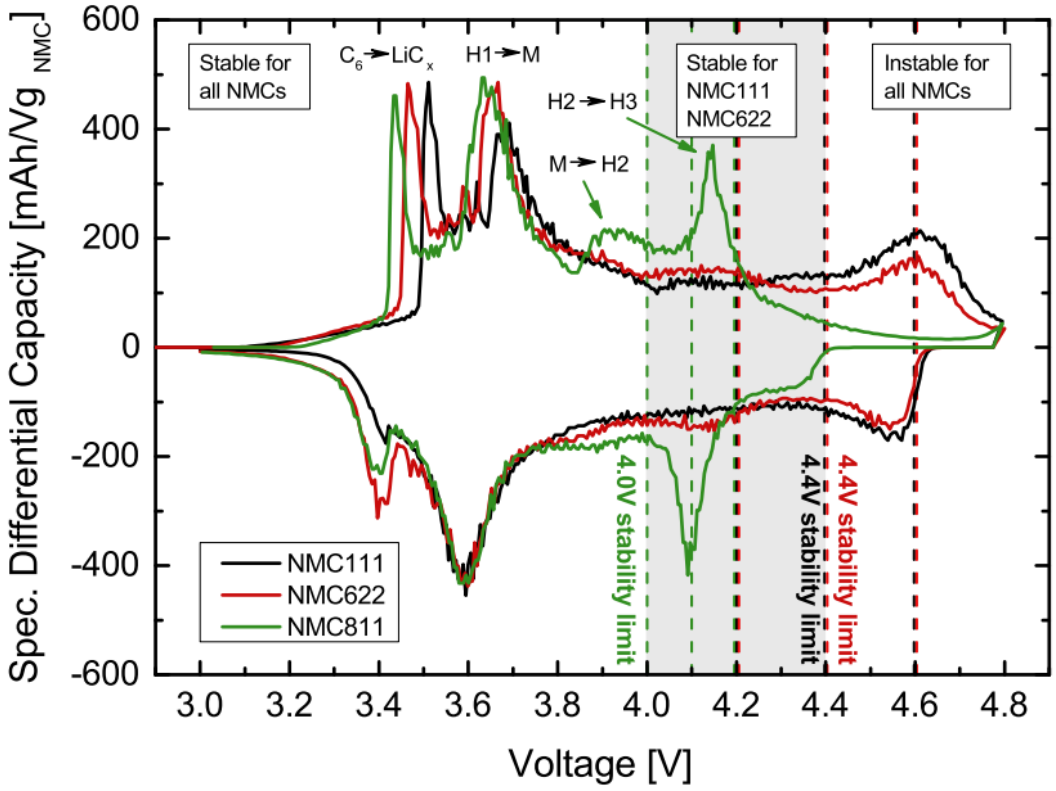

Figure 4. Differential capacity vs. cell voltage of NCM-graphite full cells, which was recorded at a 0.1C rate and 1st cycle. NCM 622 and NCM 111 has an un-obvious peak from 3.8 V to 4.6 V.[3]

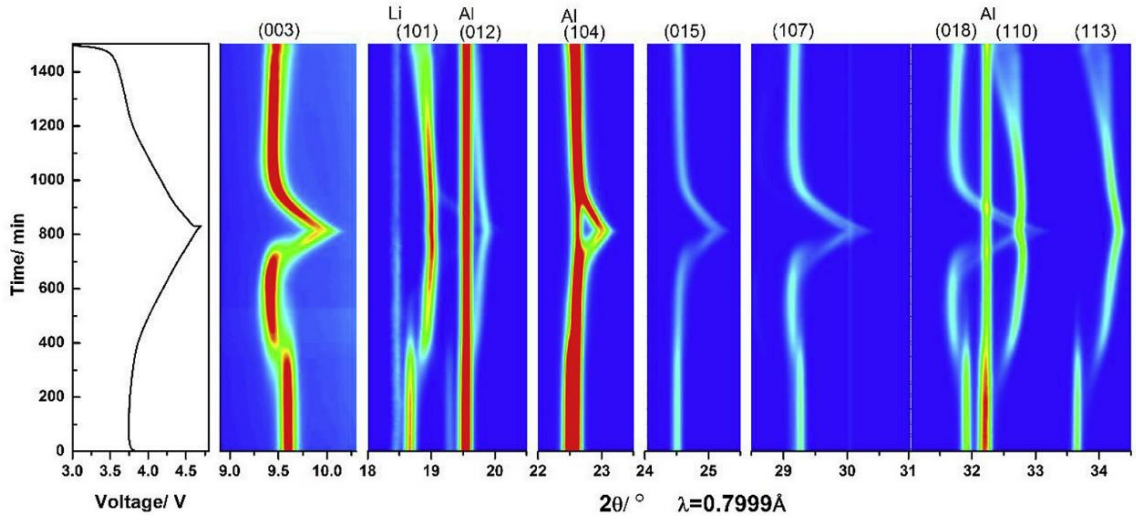

Figure 5. *in-operando* XRD with voltage profiles of NCM 622. (003), (104) are main peak related with *c*-axis and *a*- axis parameter.[4]

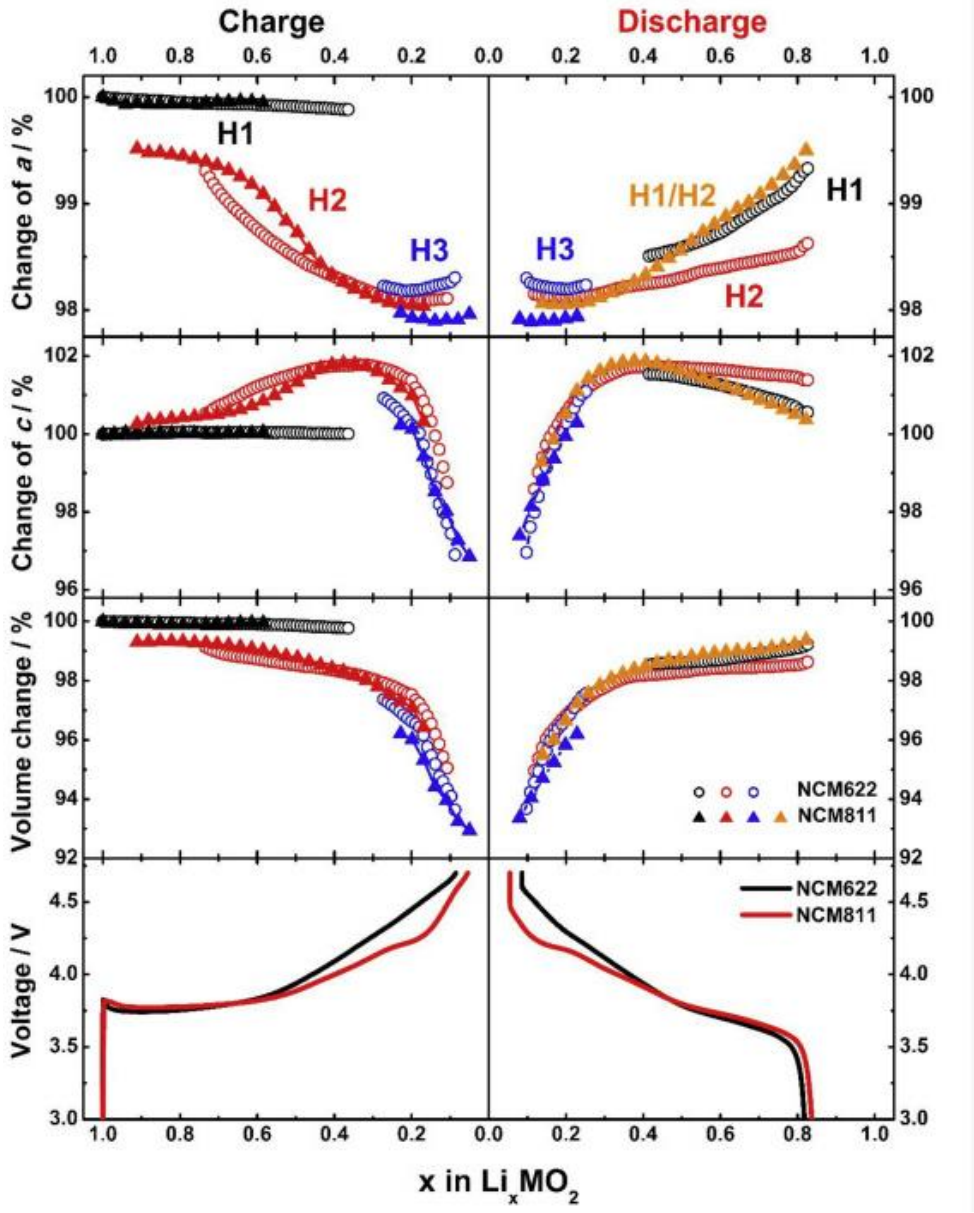

Figure 6. Comparison of lattice parameters and volume change of NCM622 and NCM811 as a function of Li contents x. The lattice parameters and volume of the pristine materials were set as 100%.[4]

Cation mixing

Ni^{2+} ions in the $LiTMO_2$ structure can easily occupy lithium sites compared to other transition metals because of their similar ionic radius with Li^+ ions. If the Ni^{2+} ions migrate to the Li sites, the layered structure transforms to the rock-salt structure, which is noted by cation mixing layer. In general, the cation mixing layer could be generated during the synthesis process and electrochemical cycling process. As the synthesis of the nickel-based cathode materials is conducted in the high temperature, $Li_{1-x}[NiCoMn]_{1+x}O_2$, a lithium-deficient phase, are partially generated due to the instability of Ni^{3+} ions.[19] The unstable Ni^{3+} ions under high temperature undergo reduction reaction for balancing electro-neutrality with releasing the xLi.[20]

An appropriate degree of cation mixing can prevent structural degradation because the nickel ions in Li slabs reduce repulsion between oxygen slabs in deep de-lithiation state.[21] However, the degree of disordering is too high or too low after the synthesis process, which can have negative effects on cell performance. When the Li/Ni cation disordering is too high after the synthesis process, lithium diffusivity is lower due to hindrance of the transition metals in the Li slabs. Likewise, low cation disordering in unit cells induces formation of spinel-like phase because of trapping manganese ions at the tetrahedral sites. As a result, inadequate cation mixed layer induces voltage decay, therefore, it is necessary that the cathode materials should have proper cation mixing layer during the synthesis process.[21]

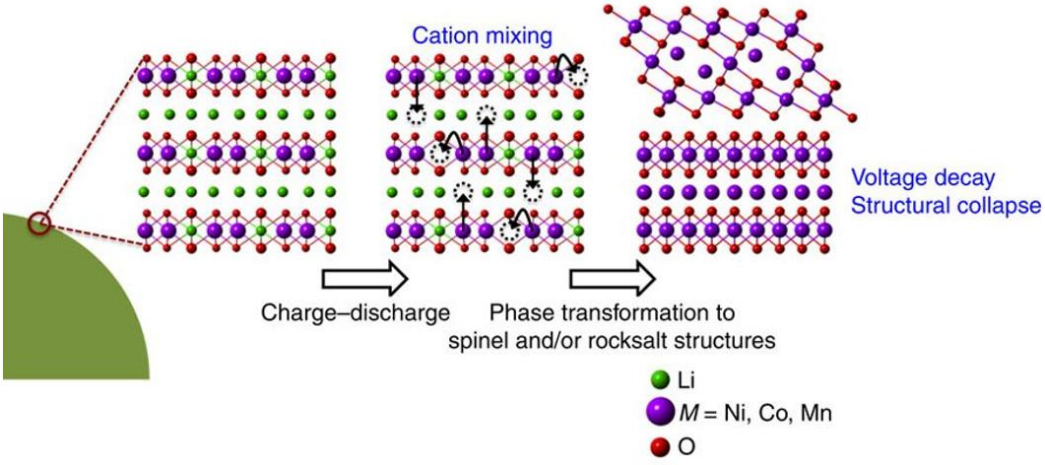

Figure 7. The schematics of the formation of cation mixing layer in layered structure.[11]

The repeated electrochemical cycling process also contribute to the formation of cation mixing layer. During the charge process, lithium vacancies are continuously generated owing to loss of

lithium ions, and they provide opportunities for movement of transition metals. Usually, the transition metals mainly occupy 3b octahedral sites, and lithium ions occupy 3a octahedral state at the pristine state. However, in order to ensure local charge neutrality and minimize columbic energy between oxygen slabs during cycles, partial Ni^{2+} ions in the TM slabs tend to glide across from 3b sites to 3a sites.[19] The phenomenon is a well-known phase transformation: layered ($R3\bar{m}$) to spinel ($Fd3\bar{m}$) and rock salt phase ($Fm3\bar{m}$). The transformed layer hinders the lithium ions migration due to the increasing surface resistance, which has negative effects on the cell performance.[6]

Moreover, the phenomena can be intensified under the high temperature. Zeng's group found that the NCM cathode materials has higher Li ion diffusivity with increasing temperature.[5] Rapid diffusivity of Li ions can realize the high capacity with elevated temperature, while the unit cells are significantly unstable and nickel ions are easily migrated to lithium site. As time passed, the cation mixing layer continuously diffuses from surface to bulk during cycles. Before the cycles, the thickness of cation mixing layer is stabilized at 2 nm, while the depth of disordered layer is at least 25 nm under high temperature (>60 °C). Consequently, the transformed layer induces surface over-potential, and accelerates capacity loss.[5-6, 17, 22]

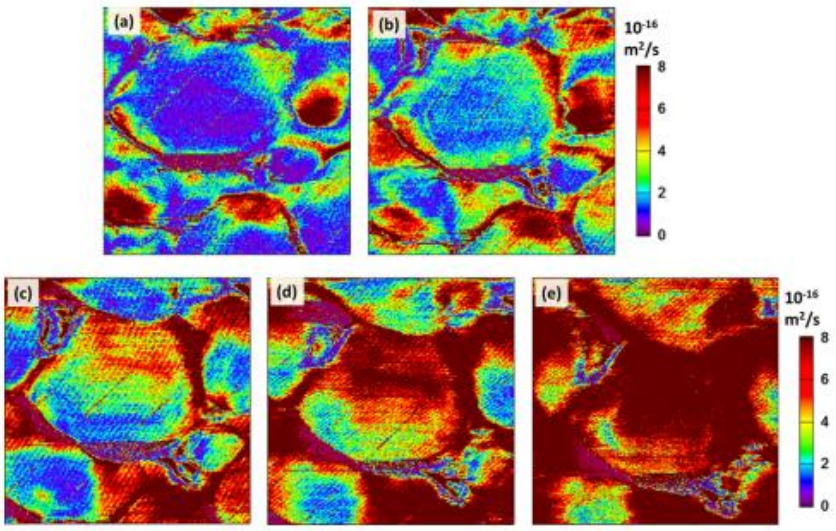

Figure 8. Electrochemical strain microscopy (ESM) images of lithium ion diffusion coefficient maps at selected temperature of (a) 25, (b) 35, (c) 45, (d) 55, and (e) 65 °C.[5]

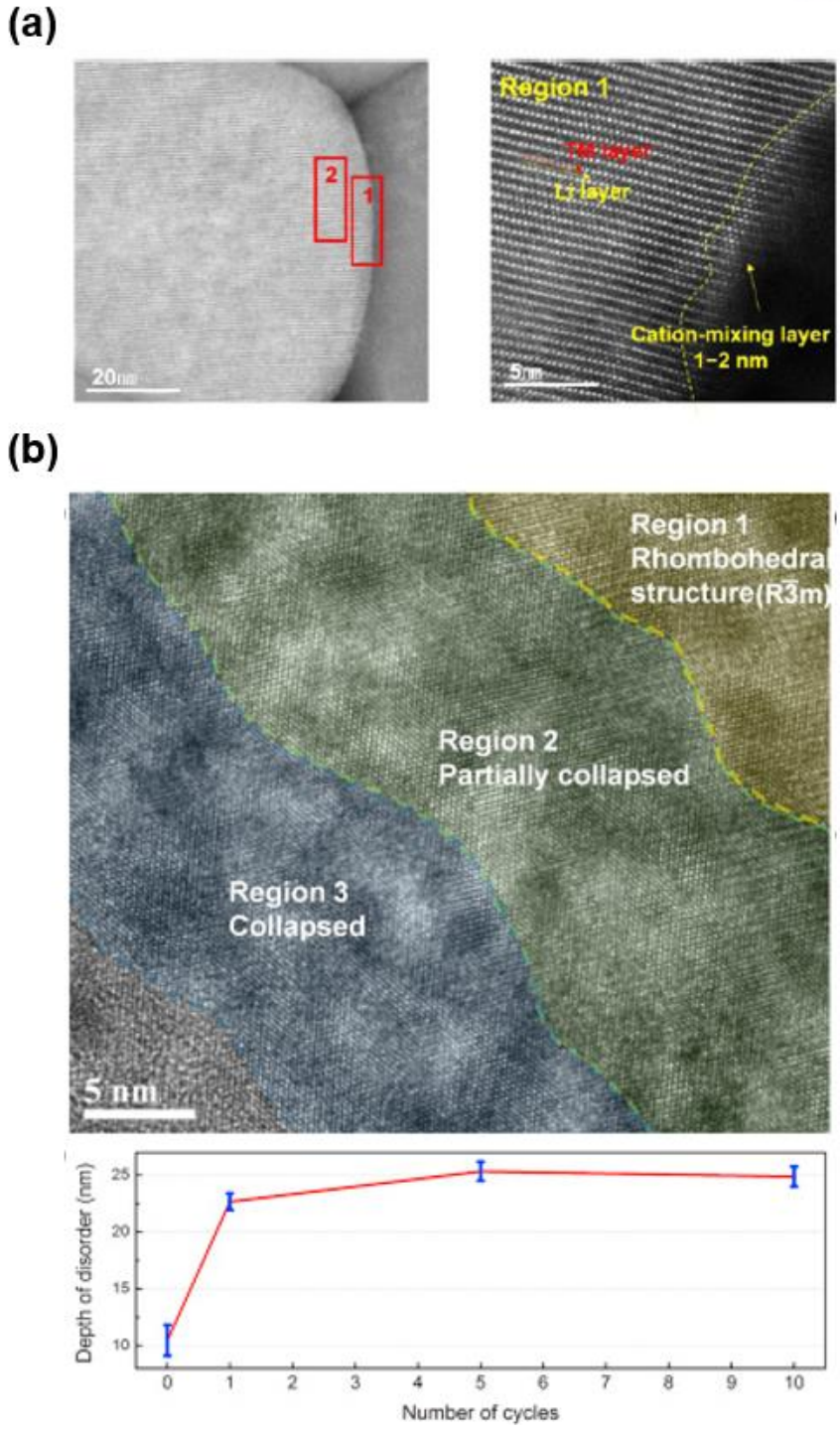

Figure 9. (a) HADDF-STEM image of the pristine NCM622 primary particles. The Region 1 shows disordering of the grain boundary. (b) HR-TEM image of the grain boundary in NCM622 cathode materials.[6-7]

Metal dissolution

$LiPF_6$ is widely used materials as the electrolyte salt in for the LIBs. The $LiPF_6$ dissociate to the Li^+ ions and the PF_6^- ions during the charge/discharge process, which provide the additional lithium and increase ion conductivity in electrolyte.[23] However, the $LiPF_6$ salts undergo not only ionization, but also the spontaneous dissociation reaction toward lithium fluoride (LiF) and phosphorus pentafluoride (PF_5). The LiF layer acts as an insulator, and it decreases lithium diffusivity. Moreover, the PF_5 molecules is strong Lewis acid, which interact with a trace of water molecules in the electrolyte. As a result, phosphorus oxyfluoride (POF_3) and hydro fluoride (HF) molecules are generated. Among the products of PF_5, the HF molecules reacts with the transition metals in surface of cathode materials. Hence, the transition metals are rapidly dissolved in the electrolyte, and the interfacial properties of the cathode materials become significantly unstable. The reaction formula is described.

$LiPF_6 \rightarrow Li^+ + PF_6^-$
$LiPF_6 \rightarrow LiF + PF_5$
$PF_5 + H_2O \rightarrow POF_3 + 2HF$ (HF formation)
$TM\text{-}O + 2HF \rightarrow TMF_2 + H_2O$ (TM dissolution)

In general, Ethylene Carbonate (EC) molecules in the electrolyte are reduced on the surface of graphite anodes, and they trap the lithium ions during charge. Therefore, open-chained EC radicals ($ROCO_2^-Li^+$) can be generated, which can initiate anionic polymerization of the EC molecules. Therefore, the organic by-products with the various chain length forms main components of the outer SEI layer during cycles. It is common reduction pathway of the SEI layer formation.

However, $LiPF_6$ salt is significantly unstable according to elevated temperature, and it is rapidly decomposed into LiF and PF_5. According to the dissociation reaction of PF_5, an excessive amount of HF molecules are rapidly generated, which induce intensified metal dissolution.[23] The dissolve metal ions move to anode surface during discharge, excessive transition metals can be placed in SEI layer compared with room temperature.

Moreover, dissolved Mn^{2+} ions on the anode surface can generate additional SEI layer through a catalytic center.[8, 24] After first charge/discharge process, the Mn^{2+} ions are rapidly coordinated with the open-chain EC byproducts due to its high reactivity of outer SEI layer, and it initiates to play the central role of the electro-catalyst. During next charge process, the linked carbonate molecules convert to alkoxide (RO^-) ions as the central Mn^{2+} ions oxidized, and release CO_2^-

radical anions.[8] The RO^- ions are final products of the inner SEI layer, so they cannot be further reduced.

Meanwhile, the generated CO_2^- radicals react with the new EC molecules, and provide the carbonate source to the Mn^{2+} center in the SEI layer. Therefore, as nearby $ROCO_2^-Li^+$ molecules replace sites of the reduced RO^- molecules, the catalytic central metals turnover. Therefore, the Mn^{2+}-carbonate complexes recover the original catalytic property. Until the open-chain carbonate molecules do not diffuse at the Mn^{2+} center, the complexes continuously generate the SEI layer. Indeed, figure 8 shows a close relation between amount of dissolved Mn^{2+} ions and thickness of the SEI layer, which clearly demonstrates that Mn^{2+} ions act as SEI layer generators.[8]

The effect of metal dissolution is easily shown according to elevated temperature.[8, 25] As the temperature increase, metal dissolution at the cathode materials could be intensified, and the radicals and lithium ions could also easily diffuse into the inner SEI layer. Therefore, the SEI layer thickly forms compared with room temperature. In this way, un-stability of the cathode material by the metal dissolution, and the excessive SEI formation on the anode surface accelerate the film resistance (R_{film}).[7, 9, 17, 24] The high R_{film} impedes movement of the lithium ions and electrons, and capacity fading of cell intensifies during cycles.

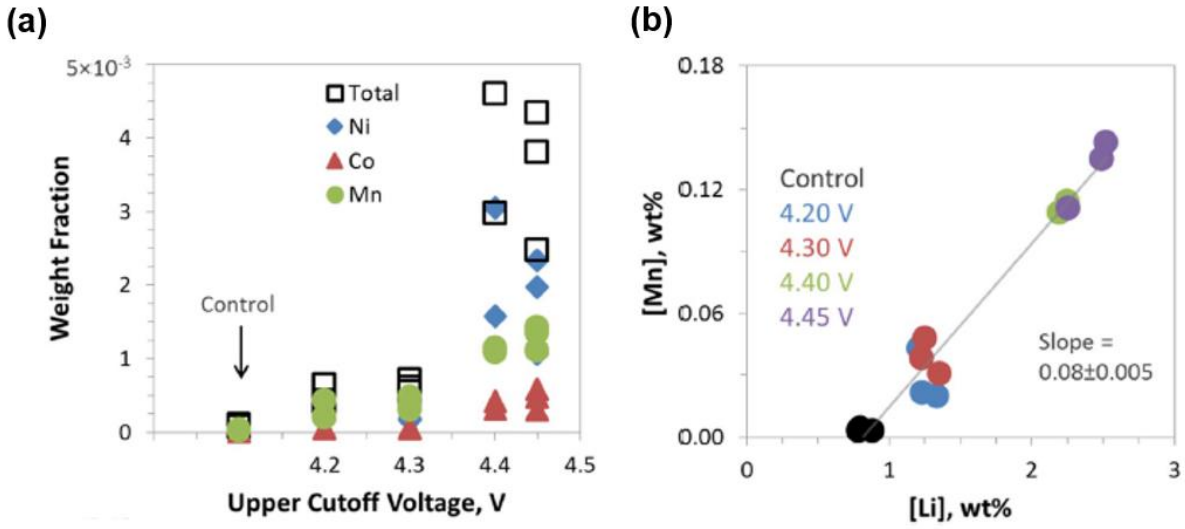

Figure 10. The graph of (a) cut-off voltage and (b) capacity loss vs amount of metal dissolution under the room temperature, which accelerated cell degradation.[8]

(a)

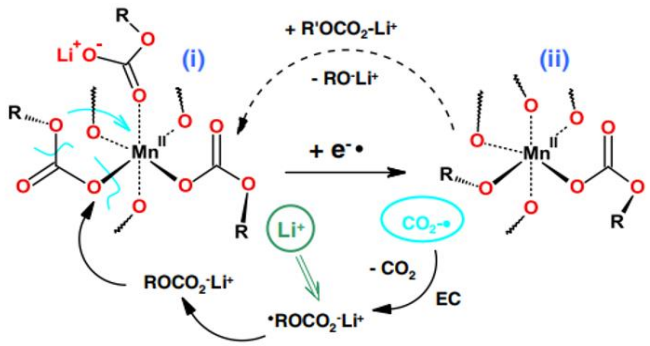

(b)

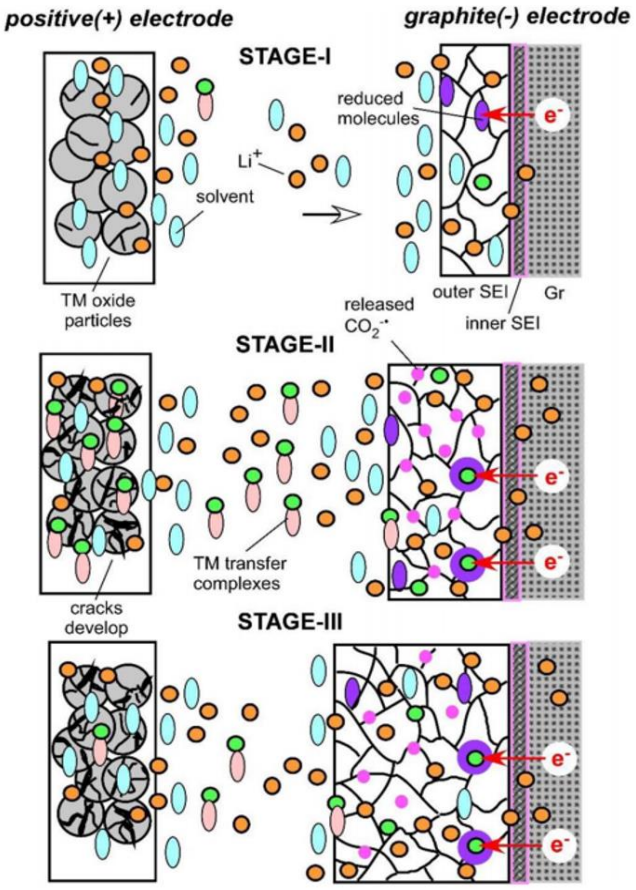

Figure 11. (a) Schematic representation for Leung's electrocatalytic mechanism for Mn^{2+} ions in SEI layer. Catalytic process shows (b) and it makes SEI layer thicker and lead to the capacity loss.[8]

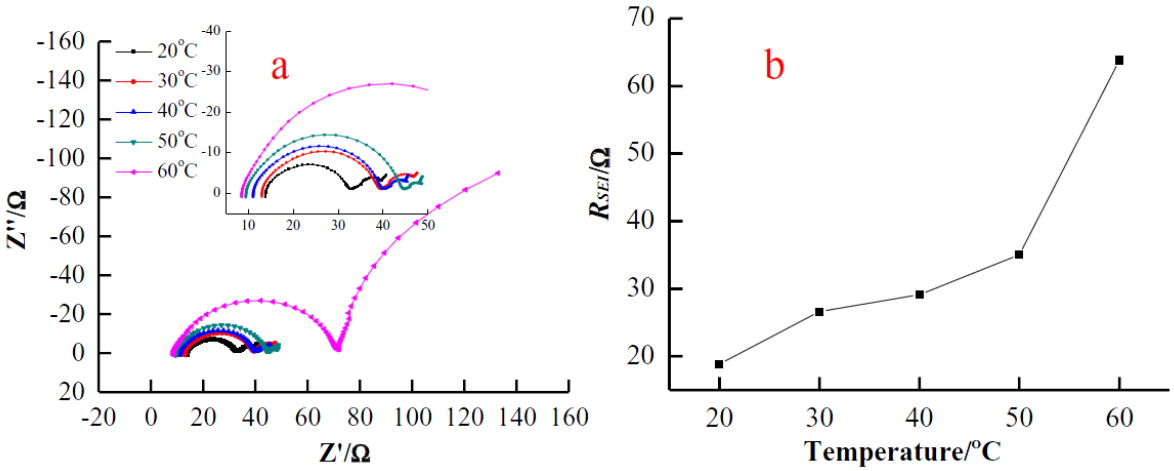

Figure 12. (a) Electrochemical impedance spectroscopy (EIS) data during the first charge in different temperature. (b) Film resistance graph of NCM cathode in 4.0 V during the first charge in different temperature.[9]

Intergranular crack/Intragranular crack

NCM cathode materials can be synthesized through a co-precipitation process, which have the structure of secondary particles. Owing to the randomly oriented primary particles, the secondary particles are considerably vulnerable to anisotropic expansion and contraction of each primary particle during cycles.[17] Therefore, the phenomena induce intergranular crack formation (Figure 13-(a)), and the NCM cathode materials undergo several negative effects as follows: (1) As the grain-to-grain connections are weaken during cycles, generation of intergranular cracks lead to the poor electrical conductivity.[17] (2) Owing to the crack formation toward the bulk, new surface is continuously exposed to electrolyte. At the fresh site, the phase transformation and side reaction rapidly occur due to the metal dissolution, which will consequently accelerate the cell deterioration.

Not only intergranular cracks, but also intragranular cracks are commonly observed in the several layered cathode materials.[10] The intragranular cracks generate in the primary particles, which are derived from un-stability of layered structure under high voltage. In figure 13-(b), at the cut-off potential above 4.5 V, defects in the layered structure are continuously generated due to the oxygen evolution, which are points to initiate formation of the premature crack. Meanwhile, as the lithium deficient cells are formed during cycles, variation of the *c*-axis lattice parameter also increases[4]. As a result, tensile stress toward *c*-axis is accumulated. In order to release internal

stress, the lithium and oxygen ions around the premature crack are preferentially removed.[10] As the defects are generated and the premature cracks are extended during charge, accumulation and alleviation of the tensile force in the primary particles can repeat during cycles. Therefore, intragranular cracks constantly grow (Figure 13-(b)).

In order to stabilize the vulnerable surface on the cathode materials, surface coating processes have been utilized, and the methods are considerably effective at the intergranular cracks.[22, 26] However, intragranular cracks cannot be prevented through the chemical processing, and the dislocations are formed at the inside of the primary particles. In order to prevent structural instability by generation of the intragranular cracks, operating voltage and rate are properly controlled, and defects of the cell should be minimized.

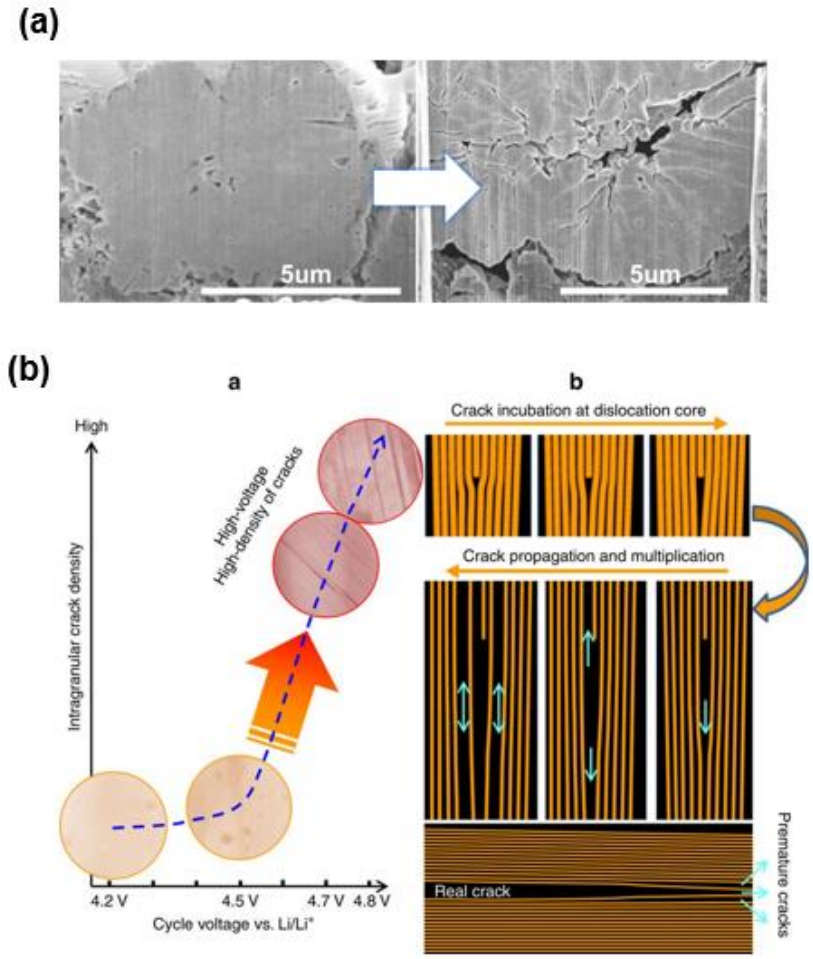

Figure 13. (a) Cross-sectional SEM images of the pristine NCM (left) and the cycled NCM (right, 100cycles at the cut-off voltage of 4.7 V) (b) The graph of the intra-granular crack density in the different cell operating voltage (left) and the schematic of crack incubation and crack propagation.[10]

1.2 Surface degradation analysis through Raman Spectroscopy

Raman spectroscopy is one of the surface analysis tools, which investigates chemical bonds with high polarizability. Therefore, the spectroscopy is suitable for the layered cathode materials because TMO_6 bonds in the layered cathodes can induce high polarizability toward external electro-magnetic field. Therefore, Raman spectroscopy can recognize the two vibrational modes of the TMO_6 bonds, A_{1g} and E_g, which are two types of the symmetric vibrational modes. (Figure 14) The A_{1g} is the stretching vibrational mode along with *c*-axis, and the E_g is the bending vibrational mode, which move in opposite directions along *a/b* plane.[11, 13, 27-28] Stretching modes are usually less stiffer than bending modes, so the A_{1g} mode is usually located at the higher wavenumber than the E_g mode.

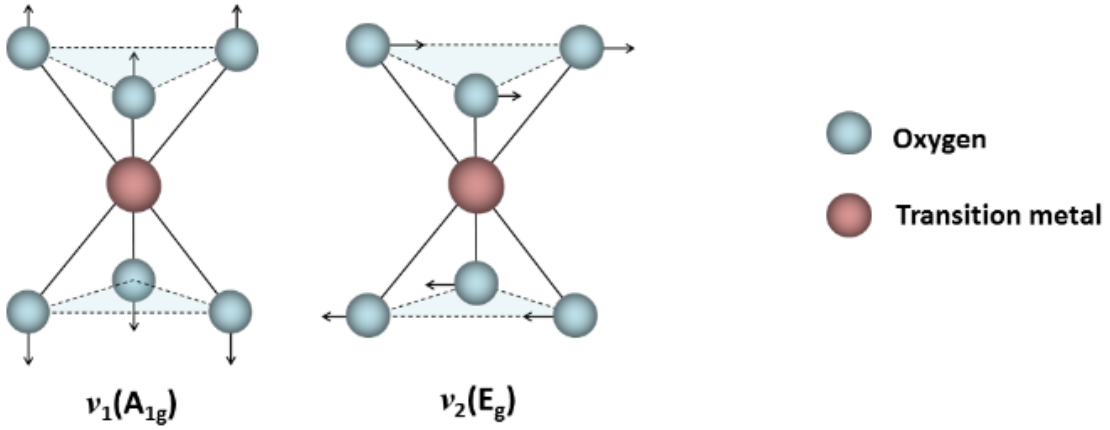

Figure 14. Schematics of the symmetric vibrational modes of MO_6 structure. Raman spectroscopy can detect the signals related with the symmetric stretching (A_{1g}) and bending mode (E_g).

NCM cathodes have six Raman peaks according to degree of freedom, which are gathered at the range between 200 cm^{-1} and 600 cm^{-1}. Therefore, in order to understand on the Raman spectra of the NCM cathodes, Raman analysis through the single layered cathode materials such as $LiCoO_2$ (LCO), $LiNiO_2$ (LNO), α -$LiMnO_2$ should be proceeded.

Figure 15 shows Raman spectra of the single layered cathode materials. In the case of LCO cathode, two Raman peaks are clearly observed at 596 cm^{-1} (A_{1g}) and 487 cm^{-1}(E_g), which are related with the symmetric vibrational modes of $Co^{3+}O_6$.[12, 29] Meanwhile, Raman spectra of the

α-$LiMnO_2$ cathode tends to be shifted toward upper wavenumber because three odd electrons in the t_{2g} orbitals induce strong polarization. Therefore, A_{1g} peak of Mn- based cathodes could appear above 600cm^{-1}.[12, 27, 30-31] In case of the LNO cathode, two Raman peaks are observed at 547 cm^{-1}(A_{1g}) and 487 cm^{-1}(E_g). In comparison with the LCO and the α-$LiMnO_2$, the LNO cathode materials can have various oxidation state of Ni ions. Therefore, LNO can have diverse degree of polarizability under external magnetic field, which induces peak broadness between 550cm^{-1} and 600cm^{-1}. Therefore, the Raman peak of the TMO_6 bonds can be predicted through the single layered cathode materials. [11]

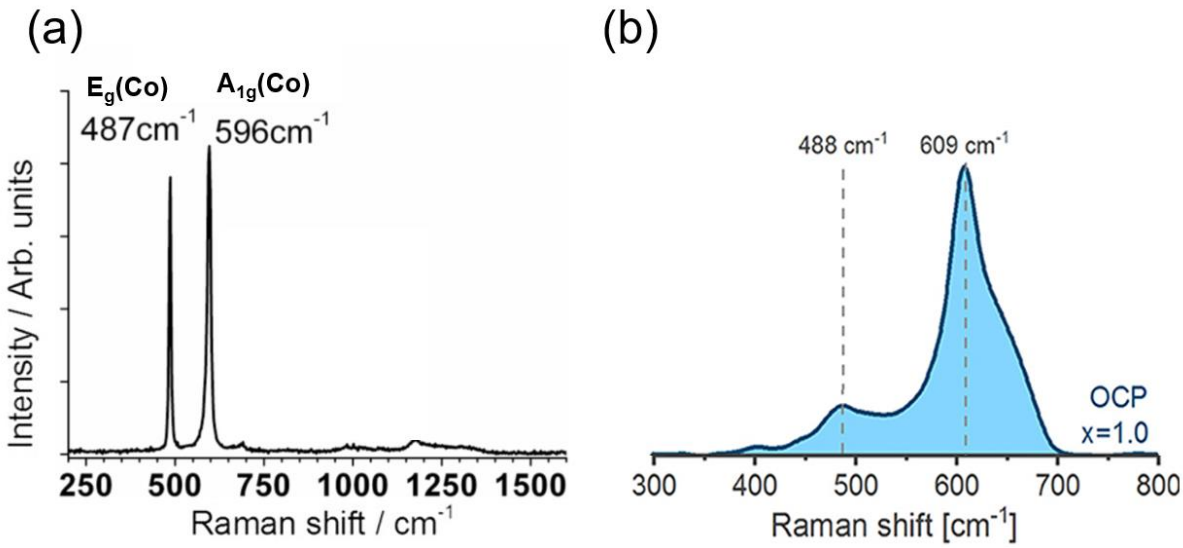

Figure 15. Raman spectra of the pristine (a)LCO cathode and (b)NCM 111 cathode.[11-12]

However, the NCM cathodes have different Raman spectra. In comparison with the single layered cathodes, the ternary NCM cathodes consist with various oxidation number of transition metals according to the ratio of transition metals, which leads to change polarizabiliy of overall TMO_6 bonds (Figure 16). Owing to the bond stiffness, E_g peaks appear at same wavenumber regardless of the transition metal ratio, while wavenumber of the A_{1g} peaks are different due to its high polarizability.

As Ni ratio in the NCM cathode increases, growth of new A_{1g} peak (548cm^{-1}) can be observed, which is related with the Ni oxidation state. Nickel ions in the NCM 111 cathode tend to have low oxidation state, however, as the nickel portion in the NCM cathodes increases, nickel ions are liable to exist in high oxidation state due to the electro-neutrality. Consequently, highly oxidized nickel ions induce decrease of polarizability, which cause A_{1g} peak to move lower wavenumber.

Indeed, the A_{1g} peak of the high nickel cathodes (Ni>0.8) matches with the A_{1g} peak of the LNO cathode, which can demonstrate that the A_{1g} peak shows polarizability of the $Ni^{3+}O_6$ bonds.[31] In comparison with the NiO_6 bonds, the CoO_6 and MnO_6 bonds have small influence on overall Raman spectra due to low degree of polarization and small portion in high nickel based cathodes.[12] Indeed, Raman peak of the ions is rarely observed at the high nickel cathodes because electrons of the Co^{4+} and Mn^{4+} are strongly trapped in d orbitals, which induce drastic decrease of polarizability.[27] Therefore, effect of the CoO_6 and MnO_6 bonds in the NCM cathodes can be negligible, and the Raman spectra can be investigated without deconvolution.[11] In conclusion, the electrode deterioration can also be measured through degree of the nickel oxidation.[32]

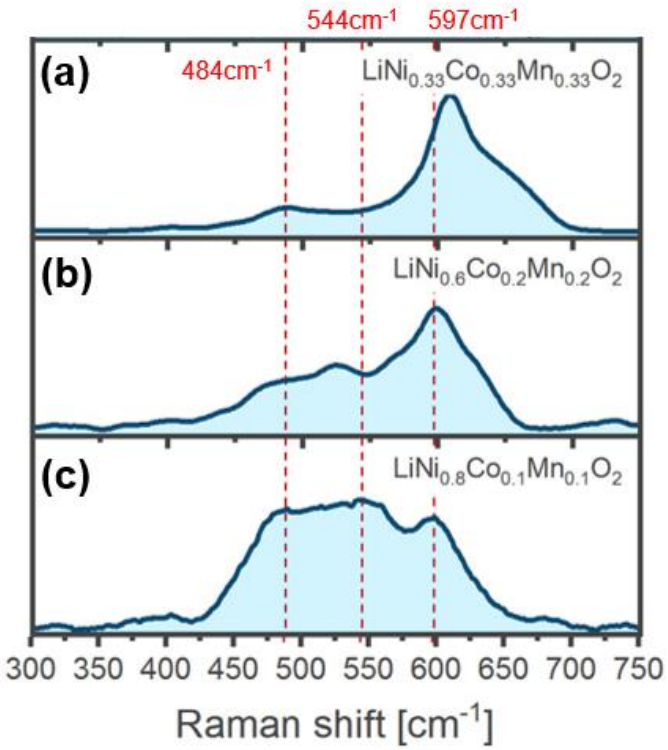

	Symmetric vibrational mode	
	A_{1g}	E_g
NCM111	610cm^{-1}	484cm^{-1}
NCM622	597cm^{-1}	484cm^{-1}
NCM811	544cm^{-1}	484cm^{-1}

Figure 16. The Raman spectra of various layered cathode materials. (a)$LiNi_{0.33}Co_{0.33}Mn_{0.33}$ (NCM111), (b) $LiNi_{0.6}Co_{0.2}Mn_{0.2}O_2$(NCM622), (c)$LiNi_{0.8}Co_{0.1}Mn_{0.1}O_2$ (NCM811).[11]

Likewise, in the basis of spectra variation according to the nickel oxidation number, variation of Raman spectra during cycles can also be interpreted. As cycle repeats, lithium ions are continuously extracted and lost due to the SEI layer formation. In order to balancing electro-neutrality in unit cell, amount of the oxidized Ni ions continuously increases in unit cell. The

accumulation of $Ni^{3+}O_6$ bonds in unit cell leads to low polarizability, therefore, A_{1g} peak of NCM cathodes continuously moves to lower wavenumber during charge.[33]

Through the properties of Raman spectroscopy, there have been attempts to investigate layered cathode degradation. Among of degradation analysis, Abraham's group tried to graft Raman spectroscopy onto cross-sectional cathode, which can observe composition of the inner secondary particles.[13] Through the method, the $A_{1g}$and E_g peaks could be clearly observed at 595 cm^{-1} and 484 cm^{-1}, respectively (Figure 17). However, as the cathode becomes lithium-deficient state during charge, repulsion force of the oxygen slabs continuously increases, therefore, the NiO_6 bonds loss its high polarizability. As a result, the new A_{1g}peak (528 cm^{-1}) are generated, while the original A_{1g} peak (595 cm^{-1}) disappears. Therefore, Raman spectra of the aged electrode shows one peak through the peak shift from the original A_{1g} peak to the new A_{1g} peak due to the nickel oxidation.

When the charge and discharge process repeats, polarizability of the TMO_6 bonds can decreases due to lithium loss, and overall Raman intensity become weaker.[11, 13, 28, 32] Therefore, electrode degradation should be measured through the ratio of A_{1g} and E_g. Through the ratio, the aged cathode has lower value of the A_{1g} and E_g than the pristine cathode because lithium loss has big influence on the A_{1g} peak intensity during cycles, while E_g peak have been little affected. Therefore, the value of the indicator continuously decreases during cycles.[13, 28] Owing to the properties of NCM Raman spectra, the cathode deterioration can be investigated through the Raman spectroscopy.

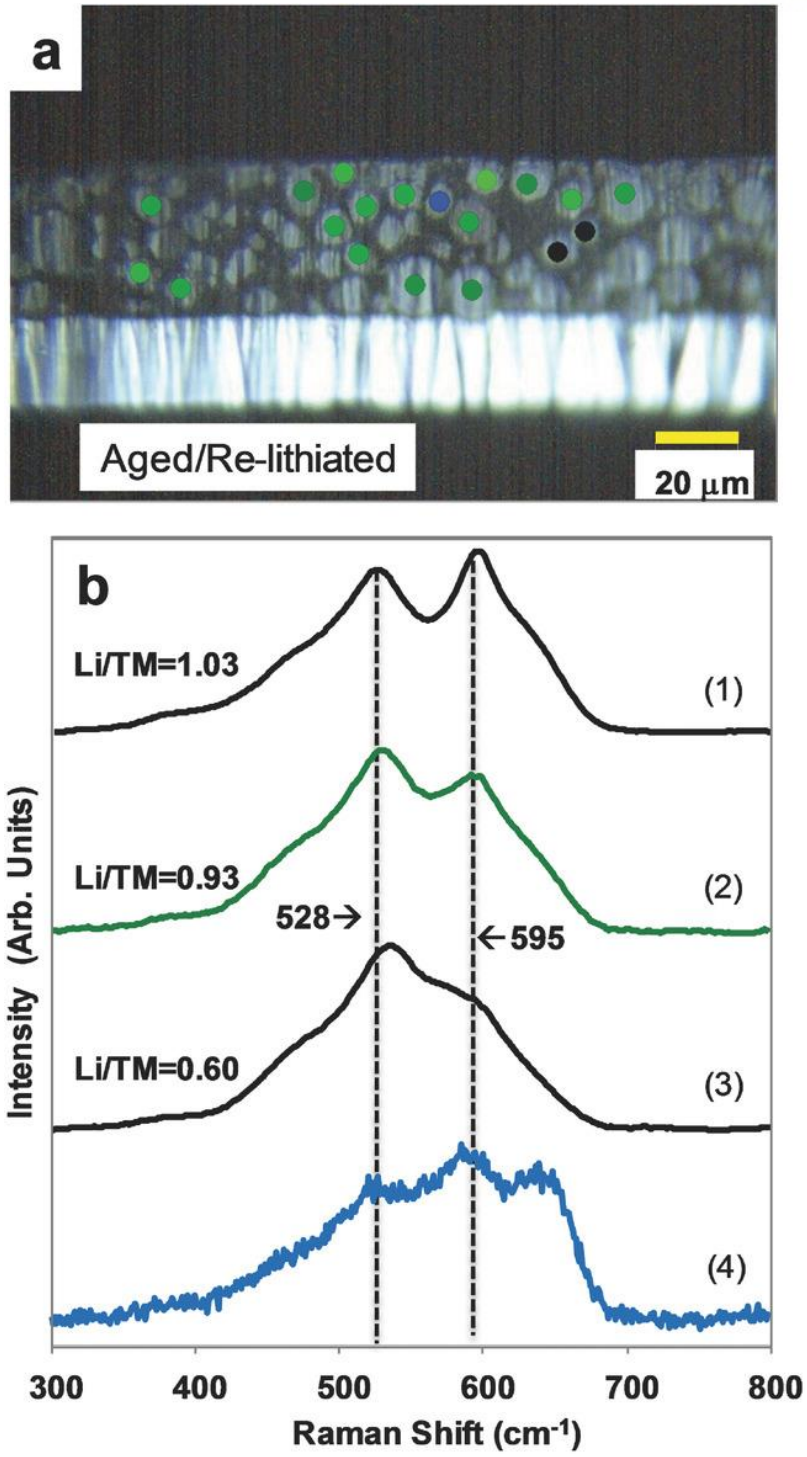

Figure 17. (a) SEM image of the cross-sectional NCM 523 electrode after 400 cycles. Raman spectra from various samples: (1) the average of the pristine electrode; (2) the average of the re-lithiated electrode after 400cycles; (3) the average of aged electrode after 400 cycles; (4) typical shape of average Raman spectra of NCM523.[13]

1.3 Objective of this works

Ni-rich cathode materials have been highlighted as future generation cathode materials, which can be introduced in the large-scale energy storage systems and electric vehicles. However, these applications accompany the huge amount of heat release, thus, the absorption of heat can accelerate battery degradation. In order to prevent the cell degradation under high temperature, majority of studies have been focused on the analysis of the cathode particle deterioration. For example, phase transition at the surface, metal dissolution, and collapse of secondary particles have been widely studied.

Although these studies have provided deterioration of cathode materials in a microscopic view, an in-depth understanding of the degradation mechanism is rarely addressed in a practical way. To meet the commercial standards of the LIBs, the electrodes are usually fabricated with a high thickness. In this circumstance, the cathode particles are placed in a variety of environment, thus, reaction inhomogeneity is indispensable in a thick electrode. Therefore, it is important to comprehend the overall degradation mechanism of the Ni-rich cathode materials under high temperature in a macroscopic level.

In the works, the secondary particle degradation *via* Raman spectroscopy with the ion-milled cathodes after the long-term cycling was measured. Raman spectroscopy is a powerful analysis tool for an observation of the degradation of the secondary particle in the electrode level. In addition, since the reference Raman data for NCM 622 is insufficient due to peak complexity, thus, the peak shift through *Ex-situ* Raman spectra during cycles intensively investigated, and the relation between lattice parameters and Raman spectra was also demonstrated. This analysis is in good agreement with the XRD and EIS results. Moreover, the ratio between original A_{1g} and new A_{1g} can suggest the degree of the local electrode degradation. In the works, the deterioration of the specific region in the bi-modal cathodes can be measured through the ratio. This study on degradation of cathodes in a macroscopic level, suggests the accurate approaches for the advanced materials to realize the superior performance.

II. Experimental section

Material selection : The small-sized $LiNi_{0.6}Co_{0.2}Mn_{0.2}O_2$ (SNCM, Cosmo AM&T) and large-sized LiNi0.6Co0.2Mn0.2O2 (LNCM, Cosmo AM&T), and bimodal distribution of $LiNi_{0.6}Co_{0.2}Mn_{0.2}O_2$ (BNCM, Samsung SDI) were prepared for the cathode materials. The artificial graphite (BTR) was prepared for the anode materials.

Preparation of the electrodes : The positive electrode was prepared by slurry casting process using 3 types of cathode materials (SNCM, LNCM, and BNCM), super P (TIMCAL), and 6wt% poly(vinylidene fluoride) binder in N-methyl-2-pyrrolidione(NMP, Daejung) with a mass ratio of 94:3:3. The slurry was mixed by a mixer at 1,500 rpm for 20 min and casted onto the aluminum foil with the loading level of ~11 mg cm^{-2}. The electrode was calendared to the loading density of 3.3 gcc^{-1}.

The negative electrode was prepared by slurry casting process using artificial graphite(BTR), super P(TIMCAL), and 1.5wt% Styrene butadiene(SBR) solution with a mass ratio of 96:2:2. The slurry was mixed by a mixer at 2000rpm for 15min and casted onto the copper foil with the loading level of 6.6mg/cm^2. The electrode was calendared to the loading density of1.4g cc^{-1}.

Electrochemical characterization : All half-cell test were performed with the 2032R type coin cell with the lithium metal as counter electrode in the Ar-filled glove box. 1M $LiPF_6$ in ethylene carbonate(EC), dimethyl carbonate(DMC), ethyl methyl carbonate (3:4:3, v/v/v) was used as an electrolyte. The graphite anode was used as counter electrode in the cointype fullcell.

The pouch-type full-cells were designed with the N/P ratio of ~1.1 using the prepared electrodes with a cathode size of 20 mm x 25 mm and an anode size of 22 mm x 27 mm. The polyethylene separator (15 μm, Celgard) was stacked between the cathode and anode.

The electrochemical performances of the half-cell were carried out in the voltage window between 3.0 V and 4.3 V using a battery cycler (WBVS-3000, WonAtech). The formation data was obtained at a charge and discharge rate of 0.1C and 0.1C and the cycle data was obtained at a rate of 0.5C and 0.5C. In terms of the fullcell, the formation was carried out in the voltage window between 3.0V and 4.2V at room temperature and formation data was obtained at a rate of C/10. The cycle data of full cell was obtained at a rate of C/3.

Charaterization **:**Ion milling System(Model 1040 Nanomill, Fischione) was utilized to obtain the cross-sectional image of the electrodes, followed by the Raman (NRS-3100) analysis.

Surface morphologies of powders and ion-milled electrodes were simply confirmed by Scanning electron microscopy(SEM,Verious 460, FEI). In addition, Energy Dispersive spectroscopy(EDS, XFlash 6130, Bruker) were utilized for element analysis before and after cycling. To analyze the degree of crystallinity of electrodes, powder X-ray diffraction(XRD, Rigaku D/MAX 2500 V/PC) was used with radiation of Cu Kα. High resolution transmission electron microscopy(HR-TEM, ARM300, JEOL) was used to investigate structural collapse of the cathode materials.

III. Result and discussion

3.1. Physical / electrochemical properties of the bi-modal NCM 622 cathode

Through the co-precipitation process, various size range of the NCM 622 cathode materials can be synthesized. In the works, the NCM cathode materials with the particle size above 8 μm is called as the LNCM (large-sized NCM, Figure 18-a), and below 5 μm is called as the SNCM (small-sized NCM, Figure 18-b). Owing to the poly-crystalline structure, the NCM particles are considerably vulnerable to the external force, thus, they undergo severe particle fractions during the calendaring process. Therefore, it has been hard to increase energy density of the uni-modal cathodes due to the particle fraction, which induce drastic side reaction during cycles. Therefore, in order to minimize particle fraction, the uni-modal cathode has been fabricated with the electrode density < 3.1 g cm^{-3}. Accordingly, the uni-modal cathodes can achieve maximized columbic efficiency (89.0% at the LNCM electrode and 91.0% at the SNCM cathode), and improved discharge capacity (175.6mAh g^{-1} at the LNCM electrode and 181.8mAh g^{-1}at the SNCM cathode, Figure 18-d,e).

However, there is a limit to increase electrode density of the uni-modal cathodes, thus, the blended cathode consisted of the SNCM and LNCM particles is fabricated, which is called as the BNCM cathode (bi-modal NCM, Figure 18-c). In comparison with the SNCM and LNCM powders, the blended cathode materials shows high pellet density at 3.89g cm^{-3}, which is a similar level of the LCO cathode materials (3.90 g cm^{-3}, Table 1). At the bi-modal NCM cathode, the SNCM particles can occupy the vacancies between the LNCM particles, thus, it can realize higher electrode density than the uni-modal cathodes. Therefore, through simply mixed two types of cathode materials, the BNCM cathode can increase electrode density although the uni-modal NCM cathodes and the bi-modal NCM cathode consist of the same NCM cathode materials. As a result, through the blended method, volumetric energy density of the NCM 622 cathode can be greatly increased from 1986 W L^{-1} to 2365 W L^{-1} (Figure 18-g).

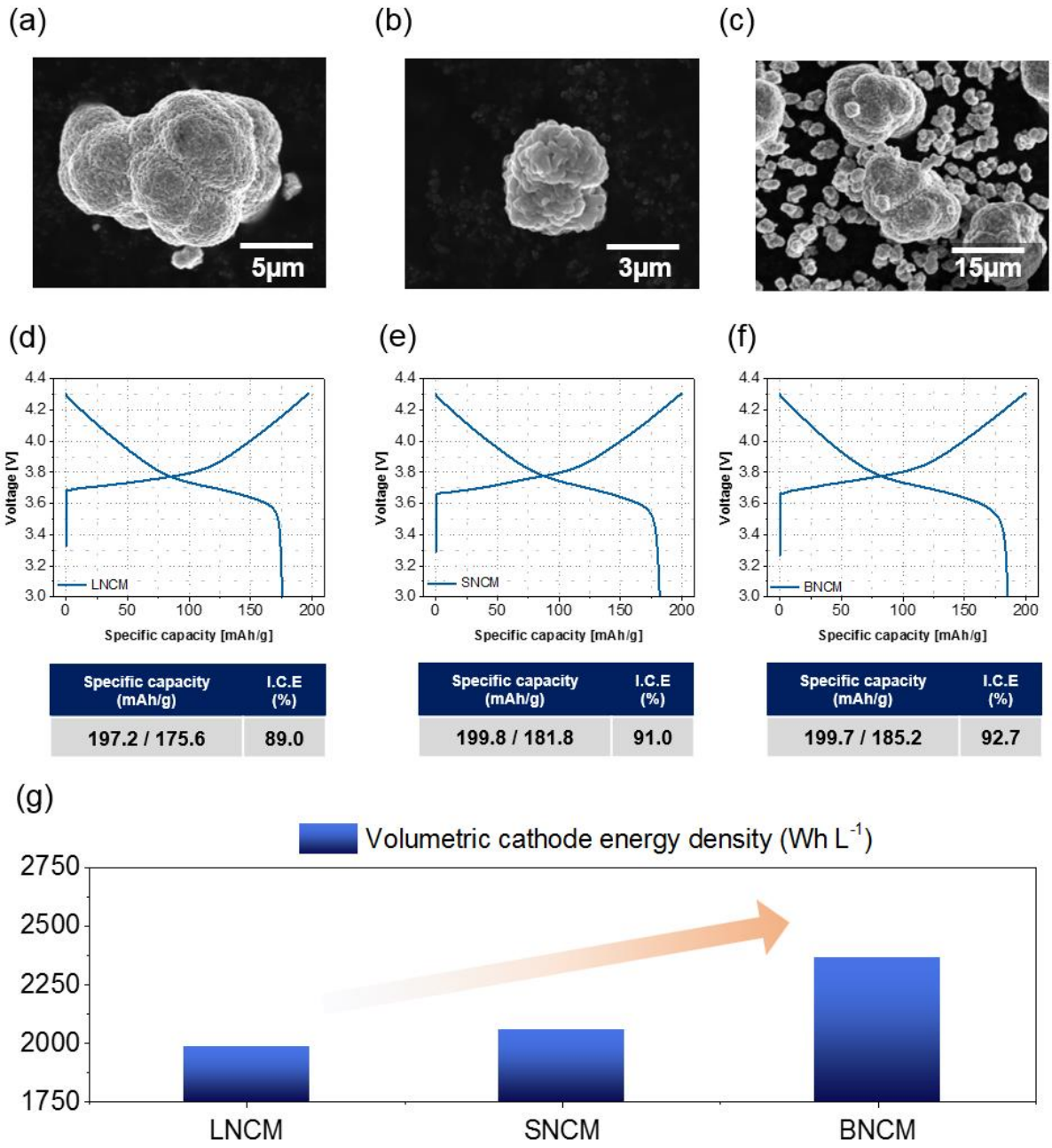

Figure 18 . Scanning electron microscopy (SEM) images of uni-modal and bi-modal cathode materials; (a) the large-sized NCM (LNCM) particle, (b) the small-sized NCM (SNCM) particle, and (c) the blended NCM cathode materials (BNCM). Voltage profile of (a-c); (d) the LNCM electrode and (e) the SNCM electrode at 3.1g/cc, (f) BNCMs at 3.5g/cc. The electrode density is determined by the particle fraction. (g) The volumetric cathode energy density (Wh L^{-1}) of (d-f).

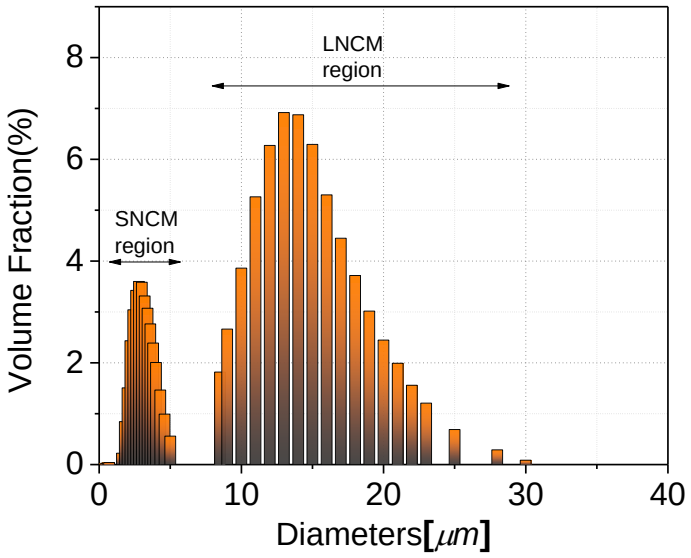

Figure 19. Particle size distribution (PSD) data of the bi-modal NCM 622 cathode. The particles below the 5um are called by SNCM, and the particles above the 8um are called by LNCM.

Secondary particle morphology	Material	Particle Size (μm)	Pellet density (g/cc)
Poly crystalline	NCM622	SNCM (1.5 ~ 5)	3.47
		BNCM	3.89
		LNCM (8.5 ~ 30)	3.76
Single crystalline	LCO*		3.90

Table 1. Pellet density of the uni-modal NCM, bimodal NCM and single crystalline LCO cathode materials. After the pellet density is measured, severe particle fraction is observed at the LNCM particles.

Moreover, the bi-modal NCM 622 full cell shows not only high volumetric density, but also outstanding cycle retention contrary to the uni-modal cathodes. In Figure 20, the BNCM cathode ensures high cycle retention of 96.9% after 250 cycles, while the uni-modal LNCM cathode was rapidly degenerated with capacity retention of 91.2%, and the uni-modal SNCM cathode also has low capacity retention of 93.4%. However, the bi-modal NCM cathode shows unstability under 45°C (Figure 21), consequently, it has inferior cycle retention of 89.0% after 250 cycles. Especially, the capacity retention of the BNCM full cell dramatically decreases during first 100

cycles, and the decrements of the capacity are stabilized after the 100 cycles. In order to improve cell stability under 45°C and extension of cycle life, it is necessary to investigate on degradation factors at the bi-modal electrode.

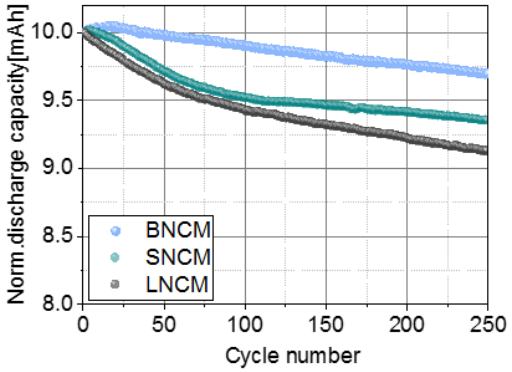

	LNCM	SNCM	BNCM
C.E(%) after 250 cycles	91.2	93.4	96.9

Figure 20. Cycle performance of the uni-modal cathodes and bi-modal cathode after 250 cycles under the room temperature.

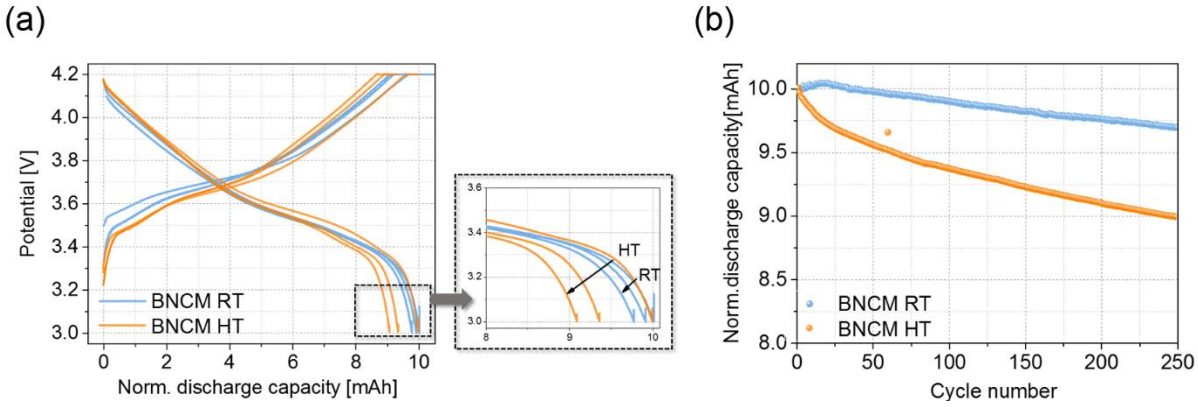

Figure 21. (a) Voltage profile and (b) cycle performance of the BNCM cathode / graphite full cell at 45°C compared with room temperature. Figure (a) shows the voltage profile about every 100 cycle.

NCM particles undergo different degradation mechanism according to the particle size, thus, bi-modal NCM cathode has complex degradation mechanism. Therefore, in order to understand on degradation mechanism of the bi-modal NCM cathode, investigation on the degradation mechanism of the uni-modal cathodes should be proceeded.

Uni-modal NCM cathode with high electrode density = 3.5g cm^{-3} has similar condition with the SNCM region and LNCM region of the bi-modal NCM cathode. In the case of the SNCM cathode with the electrode density = 3.5g cm^{-3}, large film resistance can be observed (R_{film},8.6/Ω), and low charge transfer resistance (R_{ct}, 6.0/Ω). The results show that high electrode density can induce the high film resistance at the SNCM electrodes, which may lead to deteriorate performance of the SNCM cathode. Indeed, SEM image of the SNCM electrodes shows extreme particle fractions due to the calendaring process (Figure 22-a). Corrosion of the cathode materials can increase specific surface area of the particles, therefore, side reaction between the exposed surface and electrolyte can be intensified during cycles. In this way, SEI layer on the electrode surface gradually thick, and the large film resistances can be formed. Moreover, temperature at 45°C increases lithium diffusivity, which accelerates severe cation mixing toward bulk of the SNCM particles. Therefore, particle fraction can be a main degradation factor, which leads to degenerated cycle retention at the SNCM cathodes.

On the contrary, the LNCM cathode with the electrode density = 3.5g cm^{-3} shows the lower R_{ct} (14/Ω) than LNCM cathode with the electrode density = 3.1g cm^{-3} (29/Ω). The result shows that low electrode density at the LNCM cathodes induce high charge transfer resistance. Indeed, high electrode porosity can be observed at the LNCM cathodes, which can lead to increase lithium pathway in a thick electrode. (Figure 22-b). The phenomena are caused by anisotropic expansion/extraction of the LNCM particles during cycles, which induce to separate each electrode materials. Consequently, degree of electrode porosity caused to decline mechanical strength of the LNCM cathodes, which can determine R_{ct}. High electrode density also induces high particle fraction at the LNCM cathodes but film resistance no significant differences before and after calendaring. Consequently, the particle fraction has a little influence on electrode degradation at the LNCM cathodes, while the mechanic strength among electrode materials is greatly related with the degradation of the LNCM cathodes.

In comparison with the uni-modal cathodes, the BNCM cathodes shows the higher cycle retention at 45°C, and the values of R_{film} (3.0/Ω) and R_{ct} (8.6/Ω) after 250 cycles are significantly alleviated (Figure 23). The small resistance seems to be derived from the small particle fraction in the BNCM cathode. SNCM particles move to vacancies between LNCM particles, which can prevent to contact directly among the LNCM particles during calendaring process. Therefore, SNCM particles can play a role of the buffer against the external force, thus, LNCM particles are rarely damaged, and the R_{film} also decreases. Moreover, as the SNCM particles are filled in the vacancies, binding strength among electrode materials can be strengthen during calendaring process. Lithium pathway can be shortened, thus, R_{ct} can be improved. In this way, the BNCM cathode can realize outstanding cycle performance at 45°C.

However, not only particle size, but also particle arrangement in a thick electrode can have influence on the degradation mechanism of the BNCM cathode. If each particle in the bi-modal cathode undergoes different degradation according to the particle size, the cycle retention of the BNCM cathode can be a medium level between the SNCM and the LNCM cathodes. However, the BNCM cathode has higher cycle retention than the uni-modal cathodes, which demonstrate that the particles in the BNCM cathode can have possibility undergone different degradation mechanism through the interaction with the surroundings. Therefore, it is necessary to investigate the degradation of local sites in the BNCM cathode.

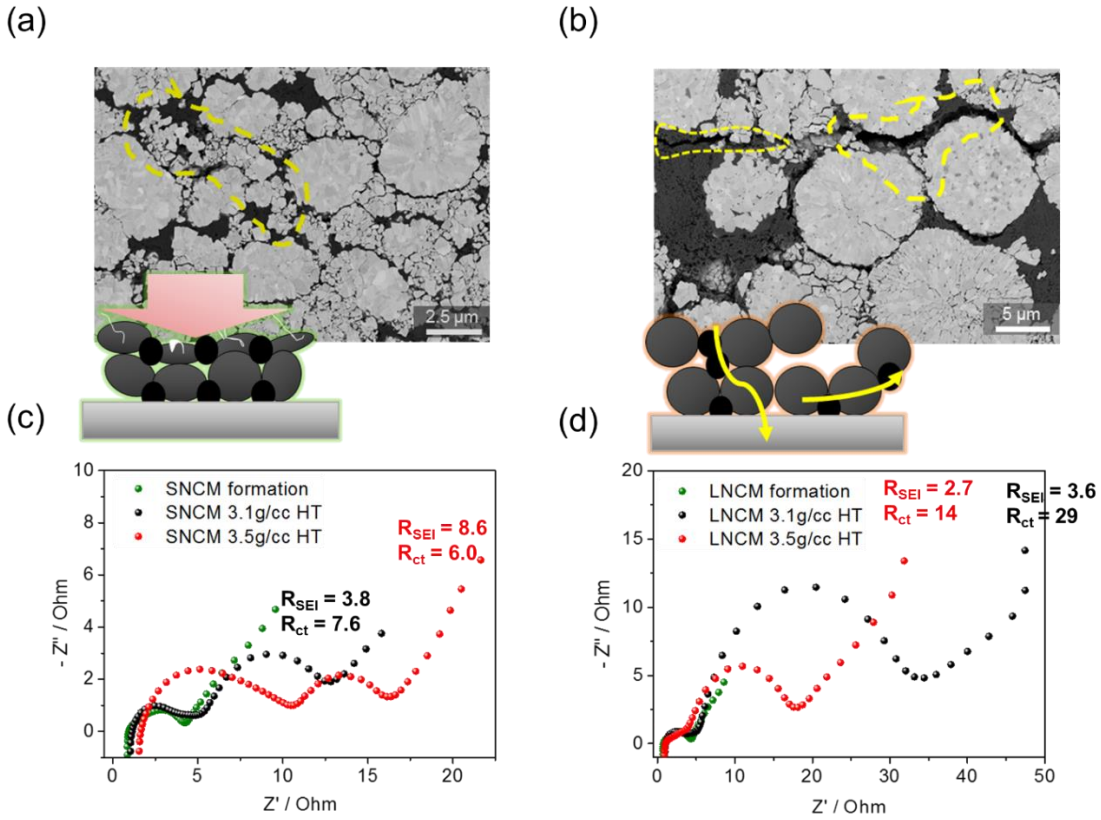

Figure 22. SEM images of the (a) SNCM cathode with the electrode density of3.5 g cm^{-3} and the (b) LNCM cathode with the electrode density of3.1g cm^{-3}. Electrochemical impedance spectroscopy (EIS, c,d) of the uni-modal cathode after the formation (green dot), and the unimodal cathode with the different cathode densities at 3.1g cm^{-3} and 3.5g cm^{-3}, after the cycle retention reached at 80% under the high temperature. (black and red dot)

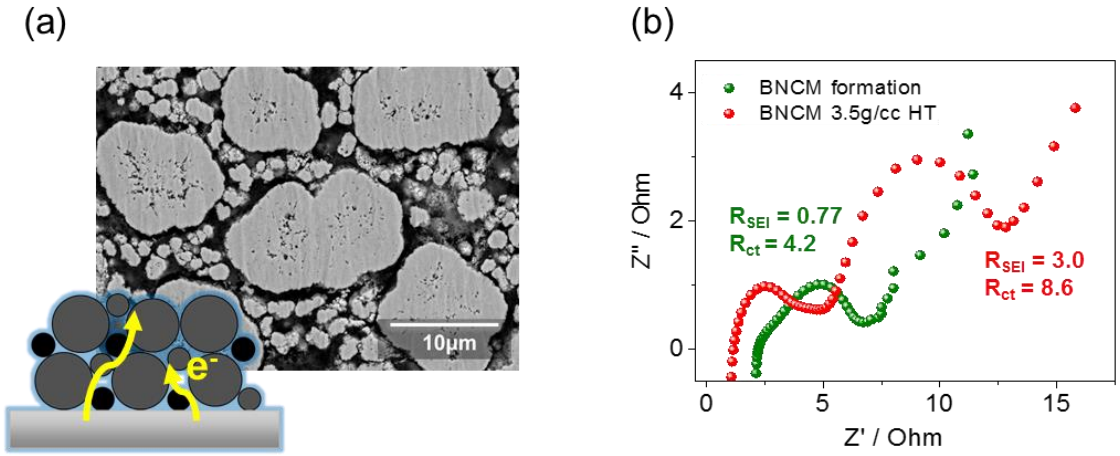

Figure 23. (a) SEM images of the BNCM cathode with the electrode density ≈ 3.5 g cm^{-3}. (b) EIS graph of the BNCM cathode after the formation (green dot), and the BNCM cathode with the electrode density ≈ 3.5g cm^{-3} after the cycle retention reached at 80%

3.2. Investigation on the local degradation through Raman spectroscopy

Raman peak analysis

Raman spectroscopy is a valuable tool for researching a structural change of layered cathode materials. Therefore, through the comparison of Raman spectra between pristine NCM cathode and aged-NCM cathode, we could be provided information about electrode degradation. However, interpretation of the NCM622 Raman spectra was considerably challenging works due to the peak agglomeration between 300cm^{-1} and 600cm^{-1}. Therefore, it is necessary to investigate on NCM cathode degradation through Raman spectral variation during cycles.

Figure 24 shows *ex-situ* Raman spectra of NCM 622 according to the operating voltage. At pristine state, an A_{1g} peak appears at 597cm^{-1}. However, as lithium ions exit during charge, the 597cm^{-1} peak is gradually diminished, and a new A_{1g} at 547cm^{-1} slightly appears. At a deep-delithiation, 4.3V, the original A_{1g} peak at 597cm^{-1} is rarely observed, while the new A_{1g} peak at 547cm^{-1} is clearly shown, which is completely different shape contrary to the pristine state. Likewise, the 547cm^{-1} peak intensity continuously decreases, and the 597cm^{-1} peak is recovered during the discharge process. However, the 547cm^{-1} peak does not completely disappears when discharge process ends, which is the result of lithium loss due to the initial irreversible capacity. In this way, the Raman spectra can have various shape according to the operating potential.

Variation of *ex-situ* Raman spectra is caused by transition metal oxidation state. At pristine state, the A_{1g} peak of the NCM622 cathode has similar position with the A_{1g} peak of $LiNi_{0.33}Co_{0.33}Mn_{0.33}O_2$ (NCM 111) cathode materials (Figure 25-). TMO_6 bonds of the NCM 111 cathode materials are consisted with two types of $Ni^{2+}O_6$ and $Mn^{4+}O_6$ bonds, which appear at 587cm^{-1} and above 600cm^{-1}, respectively. $Ni^{2+}O_6$ bonds of the NCM 111 cathode appear at similar Raman position with the NCM 622 pristine. Therefore, A_{1g} peak intensity of NCM622 can be determined by the amount of the $Ni^{2+}O_6$ bonds.

Likewise, at the de-lithiated state, 4.3V, newly generated A_{1g} peak of the NCM 622 cathode is same with $LiNiO_2$ (LNO) Raman spectra (Figure 25-a). The LNO cathode materials are consisted with the $Ni^{3+}O_6$ bonds, which appears at 547cm^{-1}. The peak at 547cm^{-1} is same with the A_{1g} peak of the de-lithiated NCM 622 cathode, therefore, the A_{1g} peak intensity of NCM 622 at 4.3V is related with the amount of the $Ni^{3+}O_6$ bonds. Consequently, through comparison with some of cathode materials, it can be demonstrated that NCM 622 Raman spectra can be determined by nickel oxidation. (Figure 25-b).

A_{1g} peaks of the MnO_6 and CoO_6 bonds in the NCM 622 cathode also appear at *ex-situ* Raman spectra. However, low contents and high oxidation number of MnO_6 and CoO_6 bonds can induce small polarizability, therefore, the MnO_6 and CoO_6 bonds have little influence on Raman intensity compared with the NiO_6 bonds. Moreover, average oxidation number of TMO_6 bonds gradually increases due to lithium loss during cycles. As a result, the polarizability of TMO_6 bonds are significantly decrease, and net contribution of the MnO_6 and CoO_6 bonds more decreases. Indeed, peak intensity of the bonds is gradually diminished without peak shift.

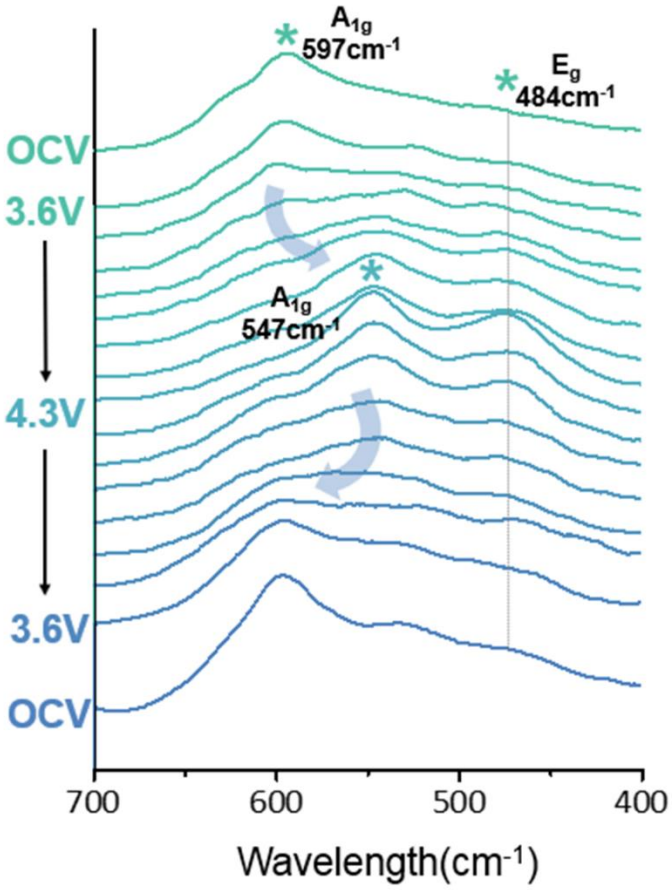

	Symmetric vibrational mode	
	A_{1g}	E_g
NCM 622	597cm^{-1} 547cm^{-1}	484cm^{-1}

Figure 24. *Ex- situ* Raman spectra of the NCM 622 cathode between 400 cm^{-1} and 700cm^{-1}

(a)

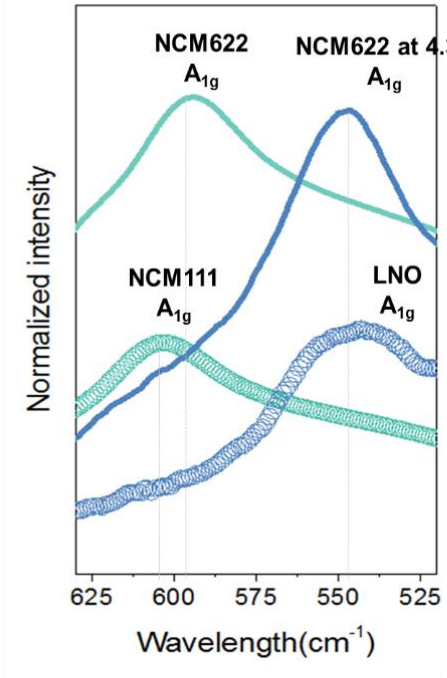

Raman peak	A_{1g}	E_g
NCM 622	597cm^{-1}	484cm-1
NCM 622 at 4.3V	547cm^{-1}	484cm-1
NCM 111	607cm^{-1}	484cm-1
LNO	547cm^{-1}	484cm-1

(b)

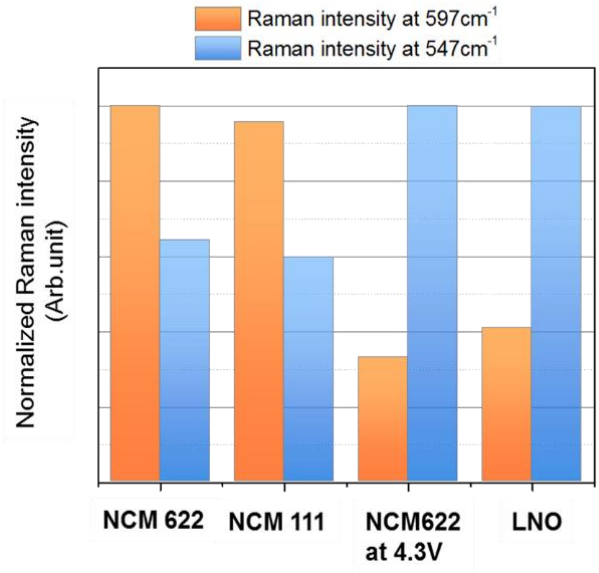

Figure 25. (a) *Ex- situ* Raman spectra of pristine NCM 622 cathode (blue green line) and de-lithiated NCM 622 cathode at 4.3V (blue line). The peaks are compared with pristine $LiNi_{0.33}Co_{0.33}Mn_{0.3}O_2$ (Blue green dot), $LiNiO_2$ (blue dot) cathode materials. (b) Normalized Raman intensity graph of (a), which can be observed at 547cm^{-1} (orange bar) and 597cm^{-1} (blue bar).

Through the peak intensity of the $Ni^{2+}O_6$ and $Ni^{3+}O_6$ bonds, cathode degradation can be demonstrated. During charge process, lithium ions in the NCM 622 cathodes gradually release, which involves in structural change. Owing to the repulsion force between the oxygen slabs, phase transition from H1 phase to monoclinic phase occurs at 3.6V, and phase transition from monoclinic phase to H2 phase may occurs between 3.9V and 4.2V. (Figure 26) When the phase transition from the H1 phase to the H2 phase occurs, *c*-axis parameter of unit cell can be increased at 1.5%, which causes considerable cell volume change. Indeed, the change of *c*-axis parameter can have influence on the bonding strength of NiO_6. As lithium ions are extracted during charge, the *c*-axis lattice parameter increases during charge, and the oxidized nickel in unit cells also increases (Figure 27). Therefore, intensity of the $597cm^{-1}$ peak extremely decreases, while intensity of the $547cm^{-1}$ increases. At a result, degree of the cathode degradation can be demonstrated by the Raman shift from $597cm^{-1}$ to $547cm^{-1}$.

Likewise, *a/b* axis parameter also can be changed by decrease of the TM ionic radius during charge process. However, in comparison with the large variation of the *c*-axis parameter, the *a/b* axis parameters are slightly changed until 4.2V because NCM 622 cathode undergoes phase transition from H1 phase to H2 phase until operating potential reaches at 4.2V. Therefore, small variation of *a/b* axis parameter have little influence on the E_g Raman peak (Figure 28). Indeed, Figure 27 shows variation of the *a/b* axis parameter and Raman intensity at $484cm^{-1}$ according to operating potential, which shows no correlation between Raman intensity of E_g peak ($484cm^{-1}$) and *a/b* axis parameter. Moreover, E_g peak is insensitive to the lattice parameter variation due to stiffness of the vibrational mode. As a result, measurement of the NCM cathode degradation through Raman spectroscopy should be proceeded by the two A_{1g} peak of NiO_6.

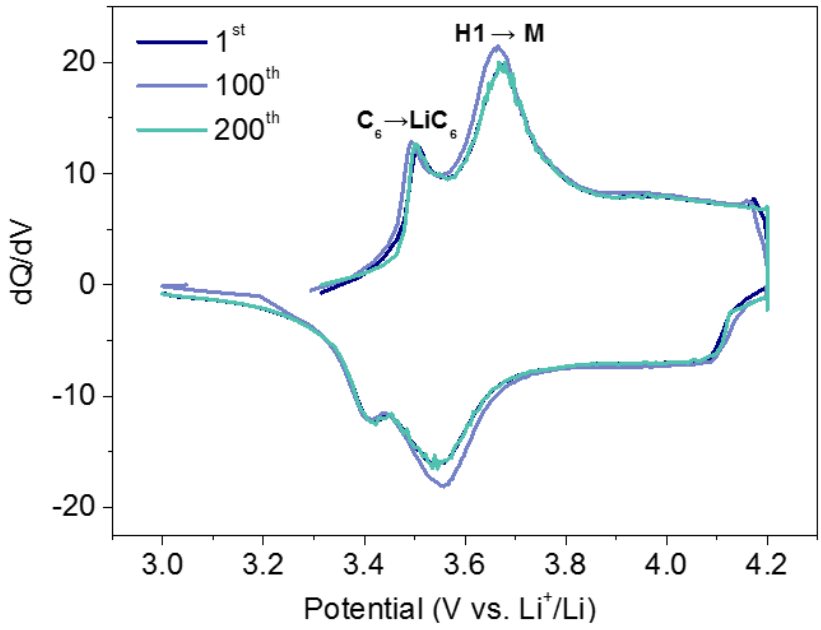

Figure 26. Differential capacity curve (dQ/dV) graph of the BNCM cathode at the 1st, 100th, 200th cycles under the high temperature.

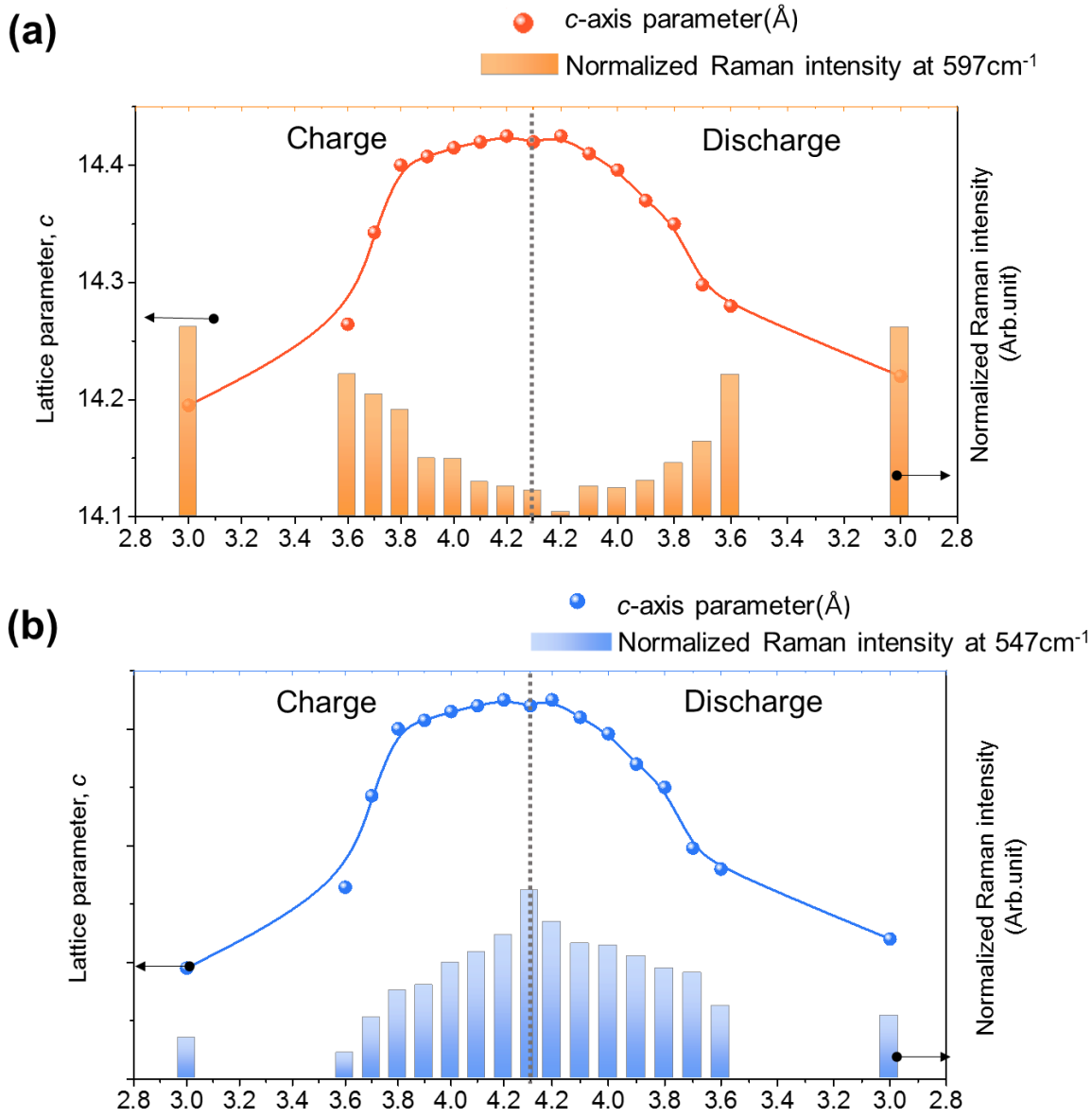

Figure 27. (a) Variation of *c*-axis parameter (orange line) and Raman intensity at 597cm^{-1} (orange rod graph) according to the operating potential. (b) Variation of *c*-axis parameter (blue line) and Raman intensity at 547cm^{-1} (blue rod graph) according to the operating potential.

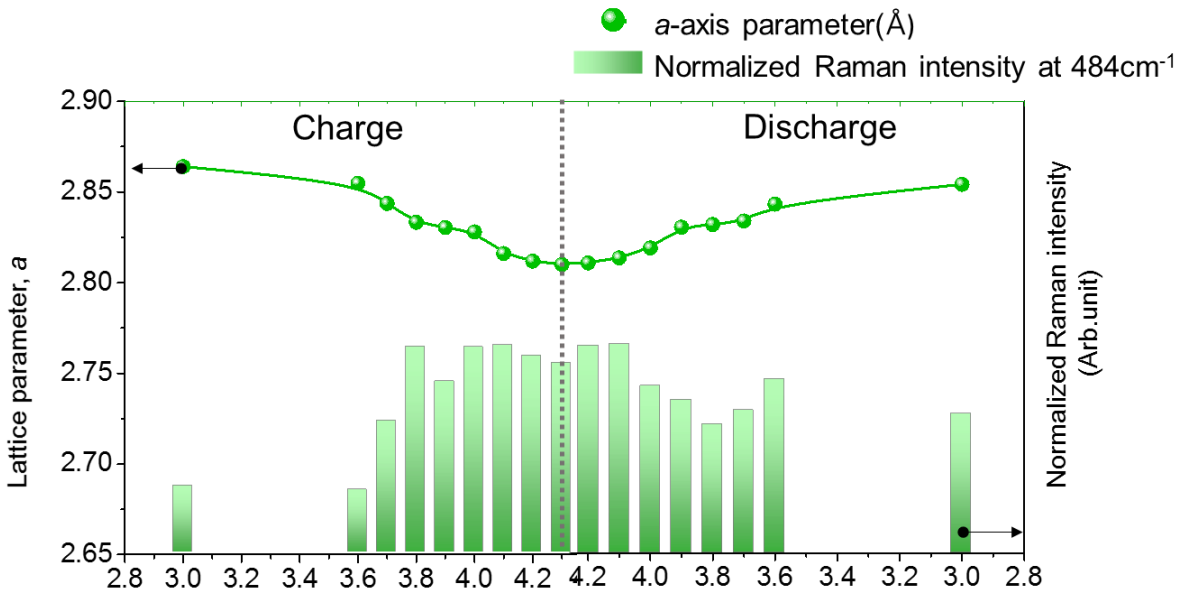

Figure 28. Variation of *a*-axis parameter (green line) and Raman intensity at 484cm^{-1} (green rod graph) according to the operating potential.

Therefore, NCM 622 cathode degradation can be demonstrated by the ratio of 597cm^{-1} (A_{1g} peak at pristine state) and 547cm^{-1} (A_{1g} peak at 4.3V). Because total amounts of nickel ions are limited, the ratio can demonstrate the overall nickel oxidation state in the NCM 622 cathodes. Figure 29 shows the $R_{597/547}$ values according to operating potential. During charge process, nickel ions rapidly oxidized, and the c-axis parameter also increases due to the intensified repulsion force between oxygen slabs. The phenomena lead to decrease polarizability of the NCM cathode, thus, the 597cm^{-1} peak is also declined.

Likewise, the NCM 622 cathodes undergo lithium insertion during discharge process, which can compensate low polarizability of the oxidized $Ni^{3+}O_6$ bonds. Therefore, Raman intensity at 597cm^{-1} can be generated again, thus, the $R_{597/547}$ value reaches 1.61 at the end of the discharge. However, it is lower value than the pristine state, which might be caused by the irreversible capacity at the formation stage. In order to compensate the charge balance by lithium loss, amount of the TMO_6 bonds remain oxidized state, which shows that they do not completely return to 597cm^{-1}. Therefore, the ratio of 597cm^{-1} and 547cm^{-1} ($R_{597/547}$) can explain the NCM cathode degradation in local sites, and it has been utilized by degradation indicator in the works.

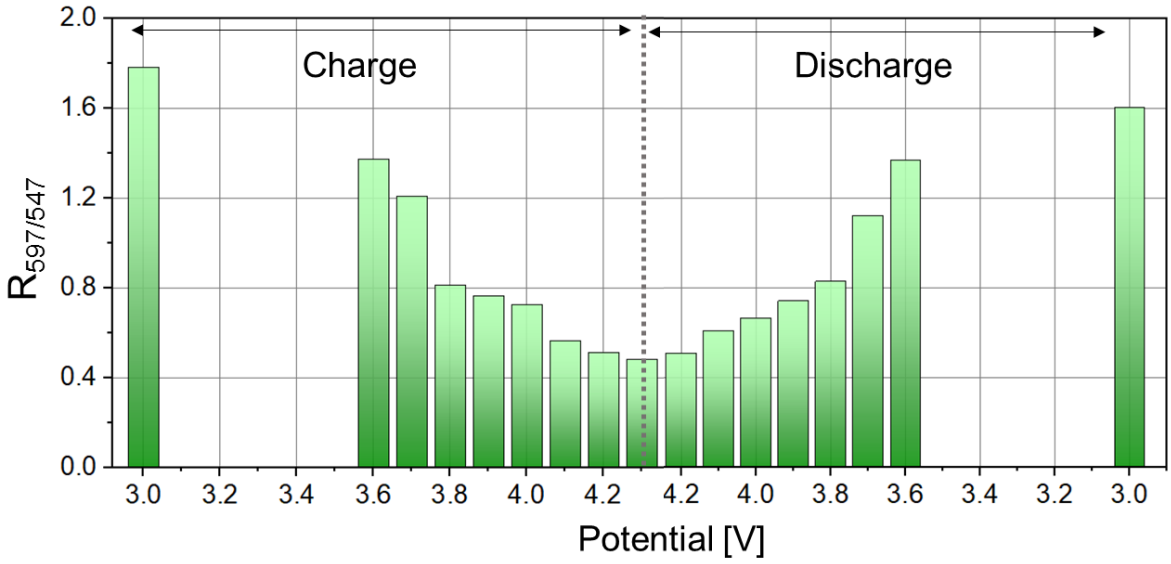

Figure 29. Degree of the NCM 622 cathode degradation represented by the $R_{597/547}$ according to the operating potential.

Investigation on degradation of bi-modal NCM 622 cathode

In order to get accurate $R_{597/547}$ values, bi-modal NCM cathode is supposed to be cross-sectioned through ion-beam. Owing to the properties of surface analysis, irradiated Raman beam cannot penetrate bulk of the secondary particles, thus, shallow penetration of Raman beam only can provide information about surface. Indeed, there is a spectral difference between the cross-sectional NCM 622 cathode and the NCM 622 cathode without ion-milling processing. (Figure 28). In the case of the NCM 622 cathode without ion-milling, boundary of the secondary particles consists with amounts of broken particles because of the calendaring effect, therefore, they can be easily exposed to the air and moisture. As a result, surface of the NCM cathode becomes lithium deficient state, which causes the peak generation at $547cm^{-1}$. Therefore, the NCM cathode has low value of the $R_{597/547}$ at 0.82. However, Raman beam irradiated cross-sectional NCM cathode can collect qualitative information throughout surface and bulk of the secondary particles. Indeed, in comparison with the electrode without ion-milling, the cross-sectional NCM cathode can have higher $R_{597/547}$ value at 1.78 and higher Raman intensity. Therefore, it is important to utilize ion-milled method for measuring cathode degradation from surface to bulk.

Through the ion-milled processing, bi-modal NCM cathode can be divided into the three regions; SNCM region is called as point 1, LNCM region is called as point 3 and blended region between the SNCM and the LNCM particles is called as point 2. The three regions are may have different degree of cathode degradation because each particle undergoes different degradation according to the particle size, and additional degradation mechanism will occur due to the interaction with surroundings. Therefore, outstanding performance of the bi-modal NCM cathode is the result of the suppressed degradation factor in local scale.

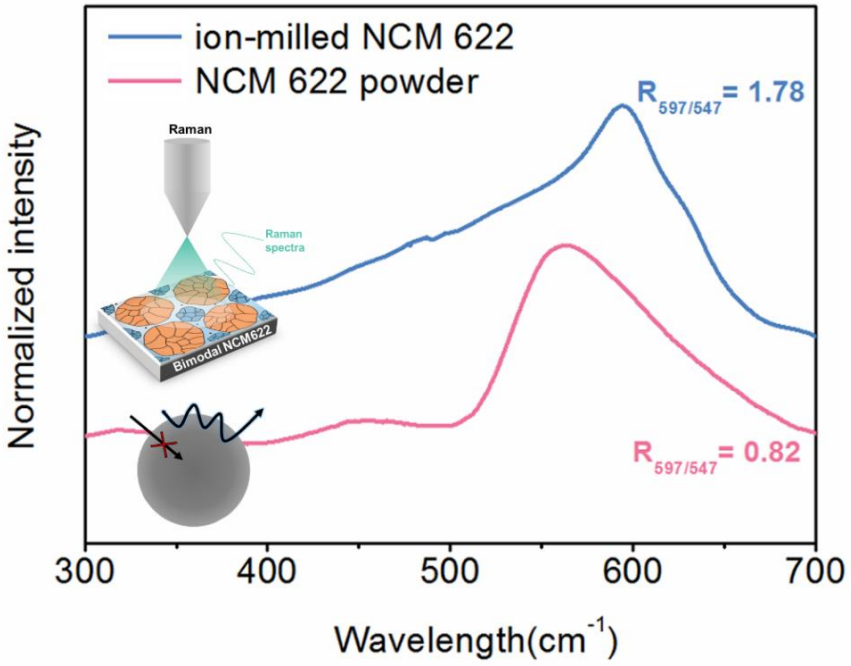

Figure 30. Raman spectroscopy of NCM 622 cathode with and without ion-milled processing (blue line and pink line, respectively)

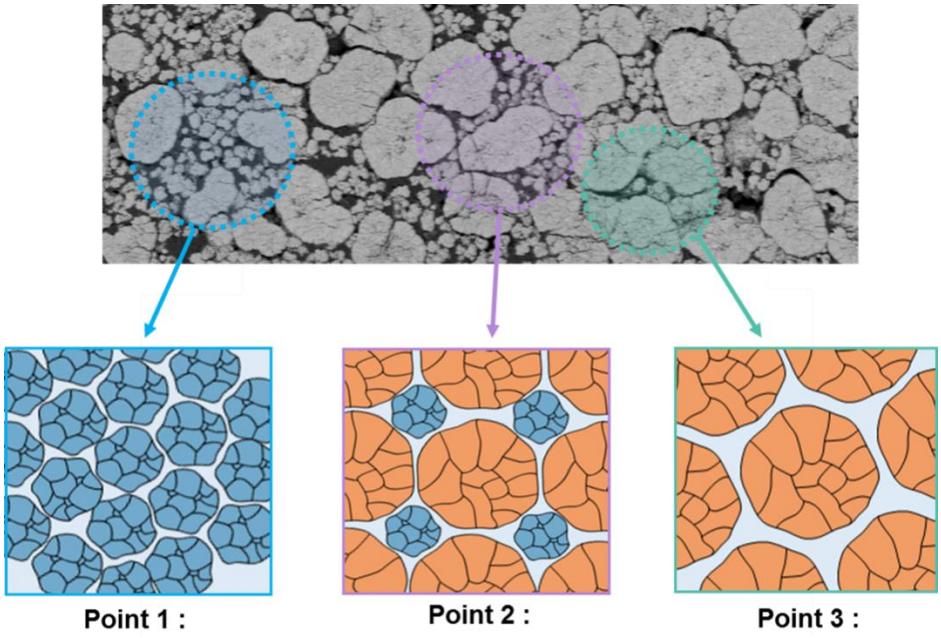

Figure 31. SEM image of the ion-milled bi-modal cathode consisted with the three points; point 1 (blue circle) is concentrated in SNCM particles, point 3 (green circle) is concentrated in LNCM particles and the point 2 is well-blended region with the SNCM and LNCM particles.

In this work, in order to compare with the electrode degradation, the uni-modal NCM 622 cathodes and the bi-modal NCM 622 cathode were fabricated. When cycle retention of the three cathodes reached around 80%, charge/discharge process would be stopped regardless of cycle number, therefore, degree of total electrode degradation among three electrodes can be identical. Point 1 and point 3 in the bi-modal NCM cathodes have similar particle arrangement with the uni-modal NCM cathodes. Therefore, if degradation mechanism similarly occurs after cycles, $R_{597/547}$ has similar value between the point in the bi-modal cathode and the uni-modal cathode. Through the comparison of the $R_{597/547}$ value, relative cathode degradation in local sites can be demonstrated.

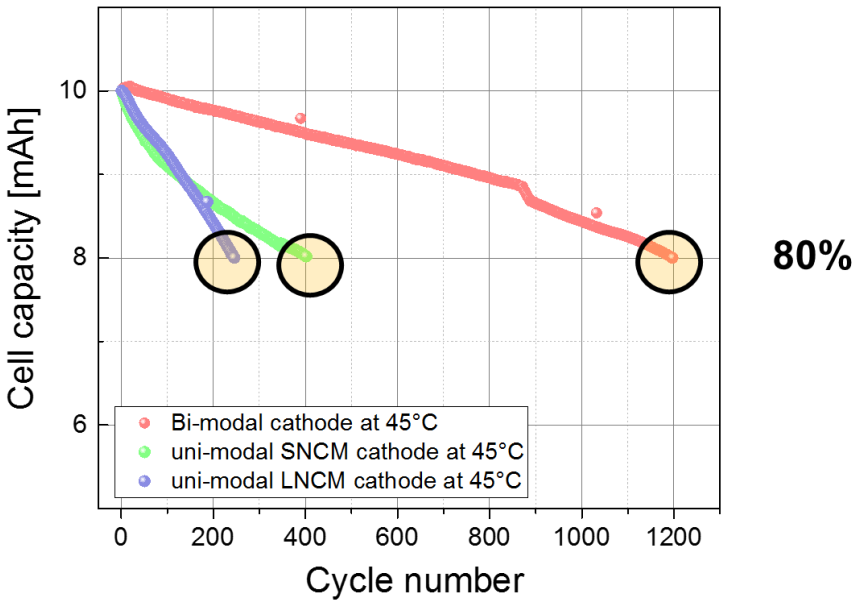

Figure 32. Cycle performance of uni-modal SNCM cathode (green point), uni-modal LNCM cathodes (blue point), and bi-modal cathode (red point) under 45°C until the cycle retention reached around 80%.

Particles in the uni-modal cathodes undergo similar electrode degradation regardless of local sites. (Figure 31) Firstly, $R_{597/547}$ value of the SNCM cathode is 1.41 after a formation stage. However, as the SNCM electrode is deteriorated during cycles, the $R_{597/547}$ value reaches at 1.22 after the cycle retention reaches around 80%, which shows that the SNCM electrode becomes shallow de-lihiated state like operating potential at 3.7V. Likewise, $R_{597/547}$ value of the LNCM cathode has 1.34 after a formation stage, which is lower $R_{597/547}$ value compared with the SNCM cathode because of the low initial columbic efficiency of the uni-modal LNCM cathode. Owing to poor cycle performance at 45°C, the uni-modal LNCM cathode rapidly reaches at cycle

retention about 80%. Despite of the dramatic electrode degradation at 45°C, the $R_{597/547}$ value of the uni-modal cathode is 1.18 after cycles, which shows that the $R_{597/547}$ values of the uni-modal cathodes commonly decrease about 14%. Therefore, when the cycle retention reaches around 80%, two uni-modal cathodes has similar degree of cathode degradation regardless of local sites.

In comparison with the uni-modal cathodes, the three points in the bi-modal cathode have different degree of cathode degradation. After a formation stage, the $R_{597/547}$ values are similar at 1.45 regardless of the points, which is the higher $R_{597/547}$ value than the uni-modal cathodes because of the lower irreversible capacity. (Figure 32) However, when cycle retention is reached around 80%, the three points show different $R_{597/547}$ values. The $R_{597/547}$ value at point 1 (SNCM region) has 1.08, which decrease by 26% compared with the end of formation state. In comparison with the rapidly deteriorated point 1, $R_{597/547}$ values at the point 2 and the point 3 undergo small $R_{597/547}$ variation before and after cycles; $R_{597/547}$ value of the point 3 (LNCM region) is 1.22, which is dropped about 15%. $R_{597/547}$ value of the point 2 (blended region) is 1.28, which decrease about 10%. The result shows that the cathode degradation at the point 1 in the bi-modal NCM cathodes extremely occurs, while blended region at the bi-modal NCM cathodes prevents cathode degradation.

Cathode degradation in local sites is determined by the degree of particles fraction. (Figure 32) During long-term cycle, every secondary particle in uni-modal NCM cathode could be collapsed due to anisotropic volume expansion of primary particles. Therefore, uni-modal cathode has similar particle degradation regardless of local sites. Likewise, in the case of the point 3, every LNCM particles is surrounded under similar condition. Therefore, the point 3 has similar degree of particle fraction and similar $R_{597/547}$ values with the uni-modal LNCM cathode. In the case of point 1, the SNCM particles lay on similar condition. However, the region has lower $R_{597/547}$ value, 1.08, than the uni-modal SNCM cathode, which is derived from the blocked lithium pathway due to the LNCM particles laid on the SNCM region. Therefore, additional degradation in the point 1 might be occurred.

At the point 2, particle arrangement seems to protect the particle fraction. (Figure 33) In comparison with the uni-modal cathode and the point 3, LNCM particles in the point 2 show small particle fraction at the central region. The undamaged local site is caused by the movement of the SNCM particles. During the calendaring process, the SNCM particles in bi-modal cathodes move to vacancies between the LNCM particles. The SNCM particles are squeezed among the LNCM particles under high pressure, thus, mechanical strength of the SNCM particles is already weaken by the external force before electrochemical reaction occurs. As a result, specific surface area of the SNCM particles extremely increases, and the SNCM

particle degradation rapidly occurs. Meanwhile, mechanical strength of the LNCM particles in the bi-modal cathode could be conserved by the movement of the SNCM particles because the SNCM particles act as a buffer against external force. Therefore, the point 2 can have higher $R_{597/547}$ value than the other points after cycles. Consequently, particle arrangement in the thick electrode can determine degree of the particle degradation.

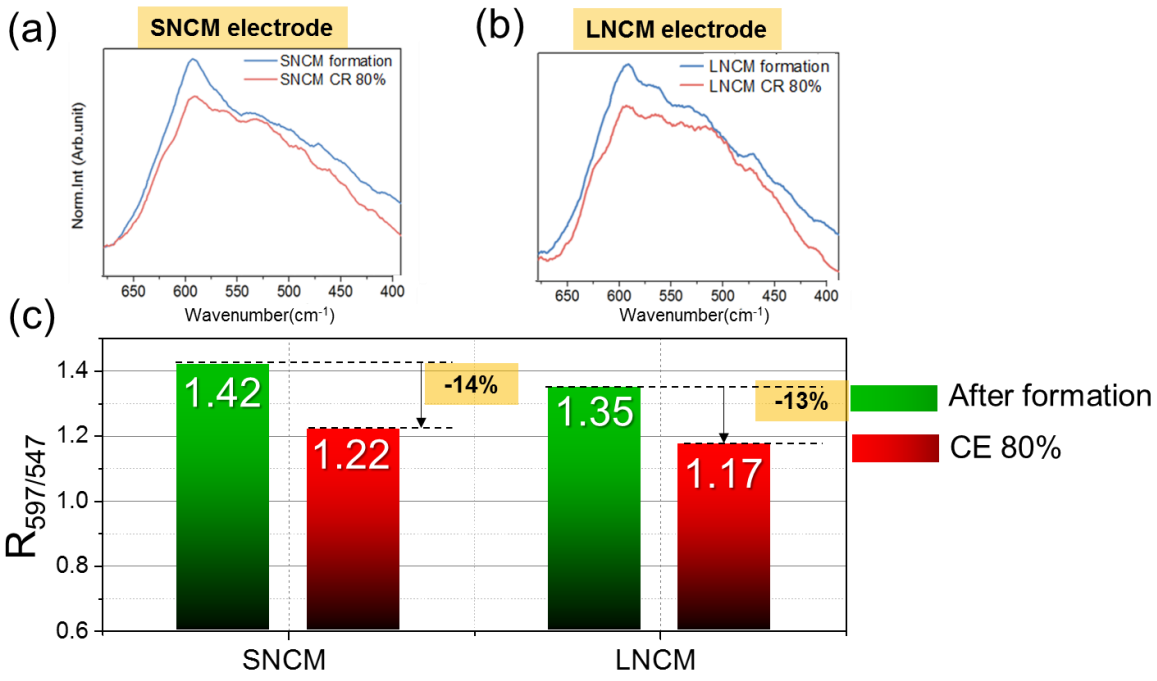

Figure 33. Raman spectra of the uni-modal NCM 622 cathodes, (a) the SNCM electrode and (b) the LNCM uni-modal cathode. The graph of (c) $R_{597/547}$ value of the each uni-modal cathode at pristine state (green bar) and cycle efficiency reached around 80% (red bar).

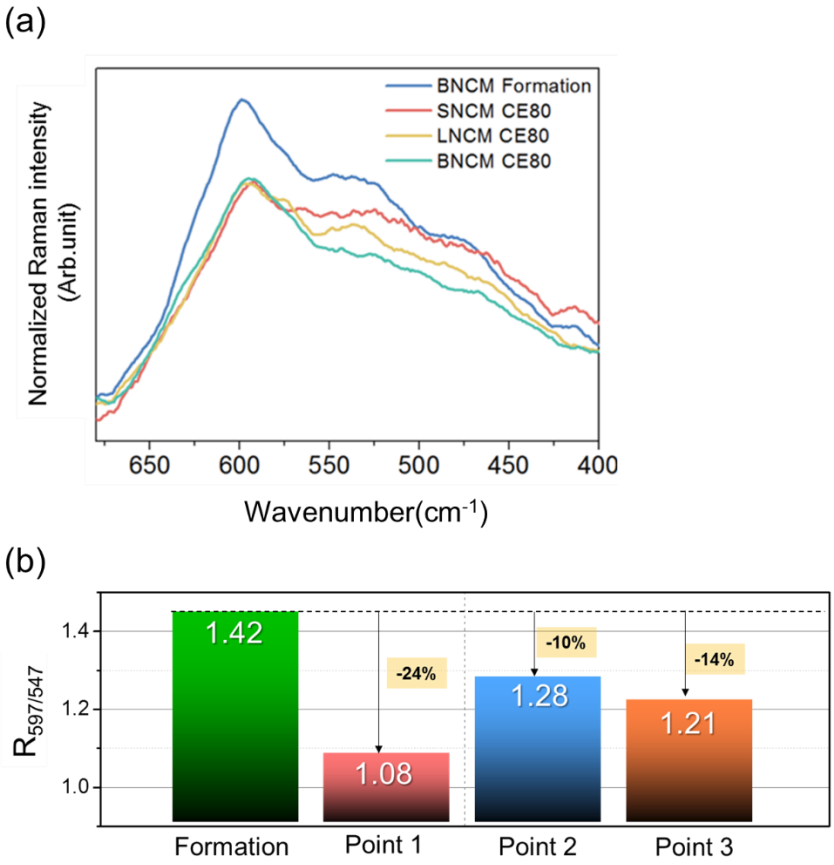

Figure 34. (a) Raman spectra of the bi-modal NCM 622 cathodes after the formation (blue line) compared with the three points, SNCM region (red line), LNCM region (yellow line) and blended region (green line) after cycle retention reached around 80%. The graph of (b) $R_{597/547}$ value after formation compared with the 3 points with the cycle efficiency reached around 80%

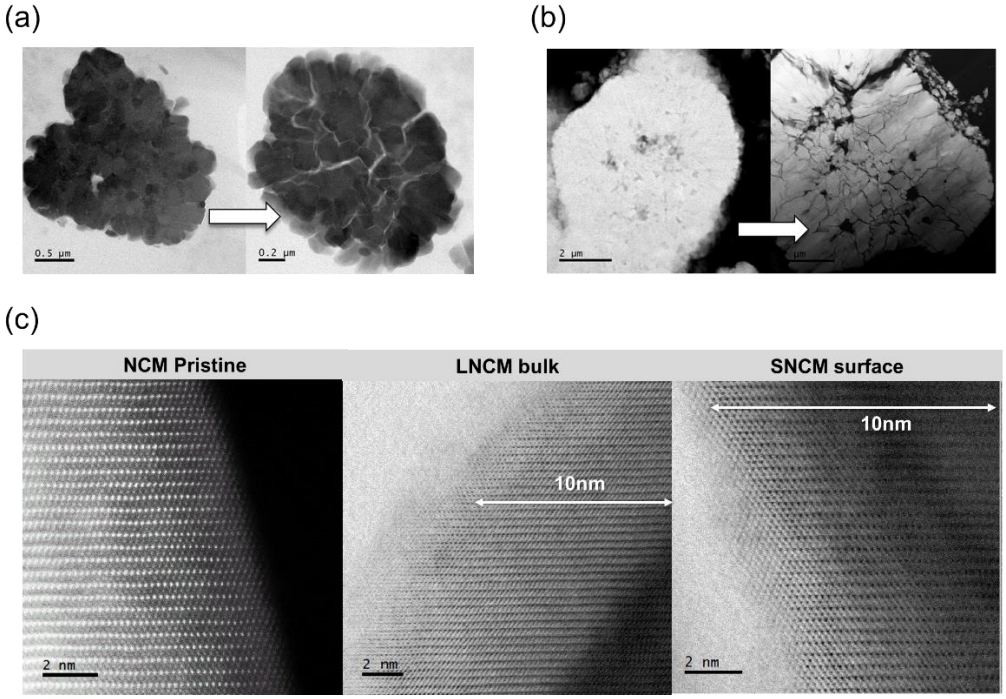

Figure 35. High resolution transmission electron microscopy (HR-TEM) images of the pristine (a) SNCM, and (b) LNCM particle in bimodal cathode. HR-TEM images of (c) cation mixing layer of the pristine NCM, bulk of the LNCM particle and surface of the SNCM particle.

3.3 Overall cell degradation mechanism derived from the cathode structural collapse

In this way, secondary structure of the NCM particles deteriorates during charge/discharge process, thus, electrolyte continuously permeate toward bulk of the NCM particles (Figure 33-1). As a result, the phenomena induce the phase conversion from R3m phase to Fm3m phase, which increase cell resistance by blocking channel of lithium ion. Meanwhile, $LiPF_6$ salt is rapidly depleted under high temperature, and the phenomena is significantly intensified during cycles (Figure 33- 2). Rapid decomposition reaction of the $LiPF_6$ salt on the surface generates amounts of HF molecules, which causes to intensify the metal dissolution. Among the transition metal dissolution, Mn dissolution seriously occurs under the room temperature, while Ni dissolution seems to be intensified under high temperature. Most of the dissolved TM ions combines with open-chain carbonate of electrolyte on the surface of anode materials. The complex can play a role of catalyst, which continuously form thick SEI layer on the anode surface. Especially, spherical SEI layers on the surface of anode materials can be observed after 600 cycles under the high temperature, which has never been observed under the room temperature. Through TOF-SIMS (Figure 33-3), composition of the abnormal SEI layer was observed, which is consisted of excessive nickel ions and F sources from decomposition electrolyte. Therefore, dissolution Ni ions may have influence on the spherical SEI layer under the condition of high temperature. Moreover, mobility of lithium ions on the surface considerably rapid at the high temperature, which induce to extract amounts of the lithium ions in unit cell. The phenomena induce high charge capacity due to the large lithium diffusivity but cycle efficiency paradoxically decreases due to loss of structure stability. Consequently, cell performance is rapidly deteriorated under high temperature.

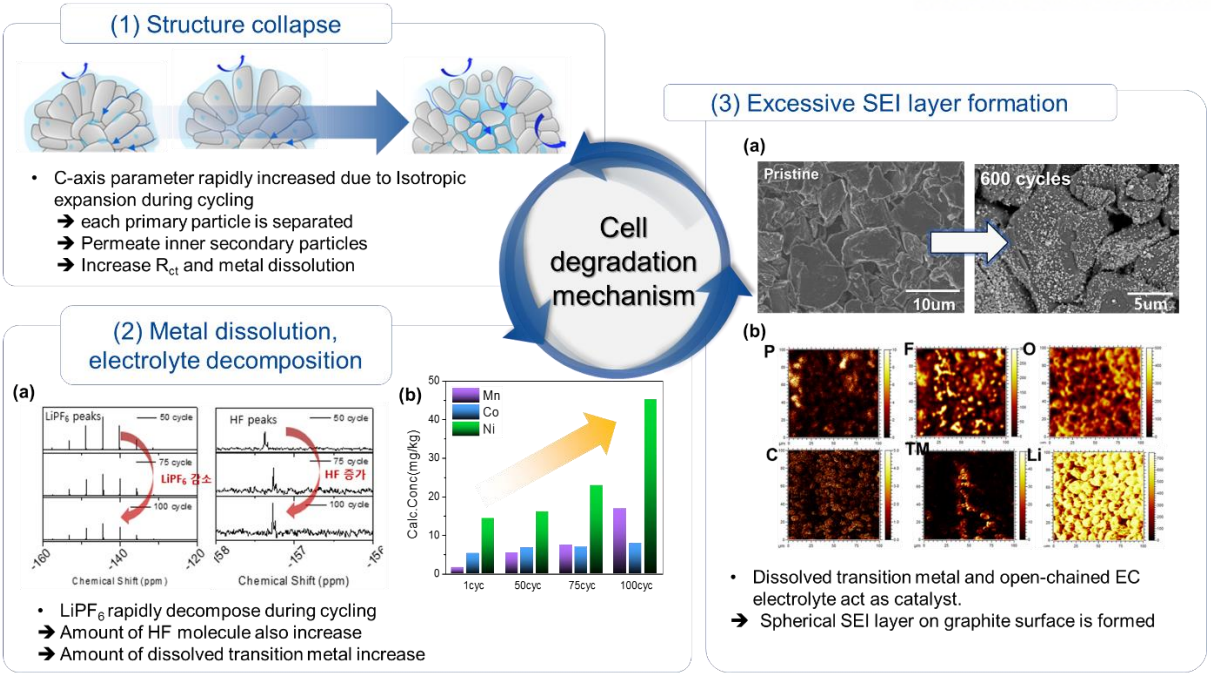

Figure 33. Overall mechanism of cell degradation under the high temperature. ^{19}F and ^{35}P-nuclear magnetic resonance spectra (NMR, 2-a) and inductively coupled plasma graph (ICP, 2-b) shown the electrolyte decomposition and the dissolved metal ions in electrolyte. SEM images (3-a) and time-of-flight secondary ion mass spectra (TOF-SIMS, 3-b) of the spherical SEI layer

IV. Conclusion

In summary, the bi-modal NCM cathode had different degradation according to the local sites, which could be demonstrated through the degradation indicator, $R_{597/547}$. In the research, point 3 (LNCM region) in the bi-modal NCM cathode has similar degree of the degradation with the uni-modal LNCM cathode. However, point 1 (SNCM region) in the bi-modal cathode undergone extreme cathode degradation compared with the uni-modal SNCM cathode. In the bi-modal cathode, SNCM particles were squeezed during calendaring process, thus, the SNCM particles were weaken before the cycles, which caused to increase the specific surface area per SNCM particles. Moreover, the LNCM particles around the point 1 blocked the lithium and electron pathway, thus, lithium loss gradually increased. Therefore, the point 1 in the bi-modal cathode undergone high electrode degradation.

However, in the point 2 (blended region), partial SNCM particles moved to vacancies among the LNCM particles during calendaring. Therefore, SNCM particles could play a role as a buffer, which could absorb external force. Consequently, the SNCM particles were fragile but LNCM particles could be preserved. Thanks to the SNCM particles, the point 2 were less deteriorate than the other site.

Therefore, in order to increase the cycle performance of the bi-modal cathode under high temperature, we suggested the three methods as follows; (1) It is necessary to increase the mechanic strength of SNCM particles because they are easy to break during calendaring. (2) Size diversification of the SNCM particle can decrease the impulse, thus, it can prevent to particle fraction. (3) The SNCM and LNCM particles in the bi-modal electrode are evenly distributed, which can decrease the electrode degradation such as the point 1 and 3. Through the improvements, the bi-modal cathode will realize superior cycle performance under high temperature.

V. Reference

1. Xue, W.; Miao, L.; Qie, L.; Wang, C.; Li, S.; Wang, J.; Li, J., Gravimetric and volumetric energy densities of lithium-sulfur batteries. *Current Opinion in Electrochemistry* **2017,** *6* (1), 92-99.
2. Mo, Y.; Guo, L.; Cao, B.; Wang, Y.; Zhang, L.; Jia, X.; Chen, Y., Correlating structural changes of the improved cyclability upon Nd-substitution in LiNi0. 5Co0. 2Mn0. 3O2 cathode materials. *Energy Storage Materials* **2019,** *18*, 260-268.
3. Jung, R.; Metzger, M.; Maglia, F.; Stinner, C.; Gasteiger, H. A., Oxygen release and its effect on the cycling stability of LiNixMnyCozO2 (NMC) cathode materials for Li-ion batteries. *Journal of The Electrochemical Society* **2017,** *164* (7), A1361-A1377.
4. Zheng, S.; Hong, C.; Guan, X.; Xiang, Y.; Liu, X.; Xu, G.-L.; Liu, R.; Zhong, G.; Zheng, F.; Li, Y., Correlation between long range and local structural changes in Ni-rich layered materials during charge and discharge process. *Journal of Power Sources* **2019,** *412*, 336-343.
5. Yang, S.; Yan, B.; Wu, J.; Lu, L.; Zeng, K., Temperature-dependent lithium-ion diffusion and activation energy of Li1. 2Co0. 13Ni0. 13Mn0. 54O2 thin-film cathode at nanoscale by using electrochemical strain microscopy. *Acs Appl Mater Inter* **2017,** *9* (16), 13999-14005.
6. Kim, N. Y.; Yim, T.; Song, J. H.; Yu, J.-S.; Lee, Z., Microstructural study on degradation mechanism of layered LiNi0. 6Co0. 2Mn0. 2O2 cathode materials by analytical transmission electron microscopy. *Journal of power sources* **2016,** *307*, 641-648.
7. Ding, Y.; Mu, D.; Wu, B.; Wang, R.; Zhao, Z.; Wu, F., Recent progresses on nickel-rich layered oxide positive electrode materials used in lithium-ion batteries for electric vehicles. *Applied energy* **2017,** *195*, 586-599.
8. Gilbert, J. A.; Shkrob, I. A.; Abraham, D. P., Transition metal dissolution, ion migration, electrocatalytic reduction and capacity loss in lithium-ion full cells. *Journal of The Electrochemical Society* **2017,** *164* (2), A389-A399.
9. Qiu, X.-Y.; Zhuang, Q.-C.; Zhang, Q.-Q.; Cao, R.; Qiang, Y.-H.; Ying, P.-Z.; Sun, S.-G., Investigation of layered LiNi1/3Co1/3Mn1/3O2 cathode of lithium ion battery by electrochemical impedance spectroscopy. *J Electroanal Chem* **2012,** *687*, 35-44.
10. Yan, P.; Zheng, J.; Gu, M.; Xiao, J.; Zhang, J.-G.; Wang, C.-M., Intragranular cracking as a critical barrier for high-voltage usage of layer-structured cathode for lithium-ion batteries. *Nat Commun* **2017,** *8*, 14101.
11. Flores, E.; Novák, P.; Jämstorp, E., In situ and Operando Raman Spectroscopy of Layered Transition Metal Oxides for Li-ion Battery Cathodes. *Frontiers in Energy Research* **2018,** *6*.
12. Inaba, M.; Iriyama, Y.; Ogumi, Z.; Todzuka, Y.; Tasaka, A., Raman study of layered rock-salt LiCoO2 and its electrochemical lithium deintercalation. *Journal of Raman spectroscopy* **1997,** *28* (8), 613-617.

13. Gilbert, J. A., Composition and Impedance Heterogeneity in Oxide Electrode cross-sections detected by raman spectroscopy
Adv Mater.

14. Placke, T.; Kloepsch, R.; Duehnen, S.; Winter, M., Lithium ion, lithium metal, and alternative rechargeable battery technologies: the odyssey for high energy density. *J Solid State Electr* **2017,** *21* (7), 1939-1964.

15. Myung, S.-T.; Maglia, F.; Park, K.-J.; Yoon, C. S.; Lamp, P.; Kim, S.-J.; Sun, Y.-K., Nickel-rich layered cathode materials for automotive lithium-ion batteries: achievements and perspectives. *Acs Energy Lett* **2016,** *2* (1), 196-223.

16. Schmuch, R.; Wagner, R.; Hörpel, G.; Placke, T.; Winter, M., Performance and cost of materials for lithium-based rechargeable automotive batteries. *Nature Energy* **2018,** *3* (4), 267.

17. Sun, H.-H.; Manthiram, A., Impact of microcrack generation and surface degradation on a nickel-rich layered Li [Ni0. 9Co0. 05Mn0. 05] O2 cathode for lithium-ion batteries. *Chem Mater* **2017,** *29* (19), 8486-8493.

18. Tian, C.; Nordlund, D.; Xin, H. L.; Xu, Y.; Liu, Y.; Sokaras, D.; Lin, F.; Doeff, M. M., Depth-dependent redox behavior of LiNi0. 6Mn0. 2Co0. 2O2. *Journal of the Electrochemical Society* **2018,** *165* (3), A696-A704.

19. Zhang, X.; Jiang, W.; Mauger, A.; Gendron, F.; Julien, C., Minimization of the cation mixing in Li1+ x (NMC) 1− xO2 as cathode material. *Journal of Power Sources* **2010,** *195* (5), 1292-1301.

20. Yoon, C. S.; Jun, D.-W.; Myung, S.-T.; Sun, Y.-K., Structural Stability of LiNiO2 Cycled above 4.2 V. *Acs Energy Lett* **2017,** *2* (5), 1150-1155.

21. Sun, G.; Yin, X.; Yang, W.; Song, A.; Jia, C.; Yang, W.; Du, Q.; Ma, Z.; Shao, G., The effect of cation mixing controlled by thermal treatment duration on the electrochemical stability of lithium transition-metal oxides. *Phys Chem Chem Phys* **2017,** *19* (44), 29886-29894.

22. Chen, Z.; Chao, D.; Lin, J.; Shen, Z., Recent progress in surface coating of layered LiNixCoyMnzO2 for lithium-ion batteries. *Mater Res Bull* **2017,** *96*, 491-502.

23. Philippe, B.; Dedryvère, R. m.; Gorgoi, M.; Rensmo, H. k.; Gonbeau, D.; Edstro¨m, K., Role of the LiPF6 salt for the long-term stability of silicon electrodes in Li-ion batteries–A photoelectron spectroscopy study. *Chem Mater* **2013,** *25* (3), 394-404.

24. Zhan, C.; Wu, T.; Lu, J.; Amine, K., Dissolution, migration, and deposition of transition metal ions in Li-ion batteries exemplified by Mn-based cathodes–a critical review. *Energy & Environmental Science* **2018,** *11* (2), 243-257.

25. Ko, D.-S.; Park, J.-H.; Park, S.; Ham, Y. N.; Ahn, S. J.; Park, J.-H.; Han, H. N.; Lee, E.; Jeon, W. S.; Jung, C., Microstructural visualization of compositional changes induced by transition metal dissolution in Ni-rich layered cathode materials by high-resolution particle analysis. *Nano energy* **2019,** *56*, 434-442.

26. Kim, J.; Ma, H.; Cha, H.; Lee, H.; Sung, J.; Seo, M.; Oh, P.; Park, M.; Cho, J., A highly

stabilized nickel-rich cathode material by nanoscale epitaxy control for high-energy lithium-ion batteries. *Energy & Environmental Science* **2018,** *11* (6), 1449-1459.

27. Ruther, R. E.; Callender, A. F.; Zhou, H.; Martha, S. K.; Nanda, J., Raman microscopy of lithium-manganese-rich transition metal oxide cathodes. *Journal of The Electrochemical Society* **2015,** *162* (1), A98-A102.

28. Zhou, F.; Cococcioni, M.; Marianetti, C. A.; Morgan, D.; Ceder, G., First-principles prediction of redox potentials in transition-metal compounds with LDA+ U. *Physical Review B* **2004,** *70* (23), 235121.

29. Reimers, J. N.; Dahn, J., Electrochemical and in situ X-ray diffraction studies of lithium intercalation in Li x CoO2. *Journal of The Electrochemical Society* **1992,** *139* (8), 2091-2097.

30. Ramana, C.; Massot, M.; Julien, C., XPS and Raman spectroscopic characterization of LiMn2O4 spinels. *Surface and Interface Analysis: An International Journal devoted to the development and application of techniques for the analysis of surfaces, interfaces and thin films* **2005,** *37* (4), 412-416.

31. Julien, C.; Massot, M., Raman scattering of LiNi1− yAlyO2. *Solid State Ionics* **2002,** *148* (1-2), 53-59.

32. Ghanty, C.; Markovsky, B.; Erickson, E. M.; Talianker, M.; Haik, O.; Tal-Yossef, Y.; Mor, A.; Aurbach, D.; Lampert, J.; Volkov, A., Li+-Ion Extraction/Insertion of Ni-Rich Li1+ x (NiyCozMnz) wO2 (0.005< x< 0.03; y: z= 8: 1, w≈ 1) Electrodes: In Situ XRD and Raman Spectroscopy Study. *Chemelectrochem* **2015,** *2* (10), 1479-1486.

33. Hwang, B.; Tsai, Y.; Carlier, D.; Ceder, G., A combined computational/experimental study on LiNi1/3Co1/3Mn1/3O2. *Chem Mater* **2003,** *15* (19), 3676-3682.